

The RAdial Velocity Experiment: Parameterization of RAVE spectra based on Convolutional Neural-Network

G. Guiglion¹, G. Matijević¹, A. B. A. Queiroz¹, M. Valentini¹, M. Steinmetz¹, C. Chiappini¹, E. K. Grebel², P. J. McMillan³, G. Kordopatis⁴, A. Kunder⁵, T. Zwitter⁶, A. Khalatyan¹, F. Anders^{7,1}, H. Enke¹, I. Minchev¹, G. Monari^{8,1}, R. F.G. Wyse^{9,10}, O. Bienaymé⁸, J. Bland-Hawthorn¹¹, B. K. Gibson¹², J. F. Navarro¹³, Q. Parker^{14,15}, W. Reid^{16,17}, G. M. Seabroke¹⁸, A. Siebert⁸

(Affiliations can be found after the references)

Received ... ; accepted ...

ABSTRACT

Context. Data-driven methods play an increasingly important role in the field of astrophysics. In the context of large spectroscopic surveys of stars, data-driven methods are key in deducing physical parameters for millions of spectra in a short time. Convolutional Neural Networks (CNNs) enable us to connect observables (e.g., spectra, stellar magnitudes) to physical properties (atmospheric parameters, chemical abundances, or *labels* in general).

Aims. We test whether it is possible to transfer the labels derived from a high-resolution stellar survey to intermediate-resolution spectra of another survey, using a CNN.

Methods. We trained a CNN, adopting stellar atmospheric parameters and chemical abundances from APOGEE DR16 (resolution $R = 22500$) data as training set labels. As input we used parts of the intermediate-resolution RAVE DR6 spectra ($R \sim 7500$) overlapping with the APOGEE DR16 data as well as broad-band ALL_WISE and 2MASS photometry together with Gaia DR2 photometry and parallaxes.

Results. We derived precise atmospheric parameters T_{eff} , $\log(g)$, $[M/H]$ and chemical abundances of $[\text{Fe}/H]$, $[\alpha/M]$, $[\text{Mg}/\text{Fe}]$, $[\text{Si}/\text{Fe}]$, $[\text{Al}/\text{Fe}]$, and $[\text{Ni}/\text{Fe}]$ for 420 165 RAVE spectra. The precision typically amounts to 60 K in T_{eff} , 0.06 in $\log(g)$, and 0.02-0.04 dex for individual chemical abundances. Incorporating photometry and astrometry as additional constraints substantially improves the results in terms of accuracy and precision of the derived labels, as long as we operate in parts of the parameter space that is well covered by the training sample. Scientific validation confirms the robustness of the CNN results. We provide a catalog of CNN-trained atmospheric parameters and abundances along with their uncertainties for 420 165 stars in the RAVE survey.

Conclusions. CNN-based methods provide a powerful way to combine spectroscopic, photometric, and astrometric data, without applying any priors in the form of stellar evolutionary models. The developed procedure can extend the scientific output of RAVE spectra beyond DR6 to on-going and planned surveys such as Gaia RVS and 4MOST.

Key words. Galaxy: abundances - Galaxy: stellar content - stars: abundances - techniques: spectroscopic - method: data analysis

1. Introduction

Stellar chemical abundances are key tracers of the star formation history of the Milky Way, and are indicators of the timing of successive star formation events. The relative chemical abundances of stars thus allow us to disentangle stellar populations and to put constraints on the nucleosynthetic origin of the respective elements Yoshii (1981); Freeman & Bland-Hawthorn (2002). It allows to constrain the composition of the gas cloud from which a star was formed and the variations of the initial mass function, particularly at the high-mass end (Wyse & Gilmore 1988; Matteucci & Francois 1989). However, in order to perform this exercise on the scale of the Galaxy, one has to observe and reduce spectra for some hundreds of thousands of long-lived stars representative of the broad kinematic, chemical and age distributions of Galactic populations (Hayden et al. 2015; Buder et al. 2019).

Over the last two decades, several efforts have been carried out to provide the community with high-quality stellar spectra, largely from dedicated spectroscopic surveys. The RAdial Velocity Experiment (RAVE) was the first systematic spectroscopic Galactic archaeology survey (Steinmetz 2003; Steinmetz et al. 2020a), targeting half a million stars. While the initial aim was to measure radial velocities of stars (Steinmetz et al. 2006), RAVE data processing was later extended to include stellar atmospheric parameters (Zwitter et al. 2008; Kordopatis et al. 2013), chemical abundances (Boeche et al. 2011; Steinmetz et al. 2020b) and Gaia proper motions (Kunder et al. 2017), thus enabling chemo-dynamical applications (Ruchti et al. 2010, 2011; Boeche et al. 2013a,b, 2014; Minchev et al. 2014; Kordopatis et al. 2015; Antoja et al. 2017; Minchev et al. 2019). Together with RAVE, the Geneva-Copenhagen survey (GCS, Nordström et al. 2004) yielded pioneering work in the comprehension of our Galaxy, based only on $\sim 17\,000$

nearby stars. The RAVE and GCS surveys were followed by numerous spectroscopic surveys with a large variety of spectral resolving power. The Sloan Extension for Galactic Understanding and Exploration survey (SEGUE, Yanny et al. 2009) obtained roughly 240 000 low-resolution spectra ($R=1800$). The Gaia-ESO survey carried out a high-resolution investigation of 10^5 stars, based on the UVES (Ultraviolet and Visual Echelle Spectrograph, $R=48\,000$) and GIRAFFE ($R=16\,000$) spectrographs of the Very Large Telescope (Gilmore et al. 2012). At a lower resolution ($R=1800$), the ongoing Large sky Area Multi-Object Fibre Spectroscopic Telescope (LAMOST) observed about one million stars in the northern hemisphere (Zhang et al. 2019). The ongoing Apache Point Observatory Galactic Evolution Experiment (APOGEE) just released their Data Release 16 (Ahumada et al. 2019). This survey observed $\sim 400\,000$ stars in both hemispheres using a high-resolution near-infrared spectrograph ($R \sim 22\,500$). GALAH (Galactic Archaeology with HERMES), an ongoing survey dedicated to chemical tagging, has targeted nearly 350 000 stars at high resolution ($R \sim 28\,000$, Buder et al. 2018) to provide detailed chemical abundances. A common feature of all these endeavors is that, owing to the sheer number of spectra, automated and eventually unsupervised data reductions and parameter determination algorithms have to be employed.

In the near future, WEAVE (WHT Enhanced Area Velocity Explorer, Dalton et al. 2018) and 4MOST (4-metre Multi-Object Spectroscopic Telescope, de Jong et al. 2019) will deliver intermediate and high-resolution observations of several millions of stars (see Chiappini et al. 2019 and Bensby et al. 2019 for details on the 4MOST low- and high-resolution surveys of the bulge and disks, respectively). The need for automatic and fast software for parameterization for stellar spectra will become even greater.

To derive atmospheric parameters and chemical abundances, standard pipelines usually compare spectral models to observations, whether localized around selected spectral lines or alternatively over a larger wavelength span. Methods range from curve-of-growth fitting of spectral lines (e.g. Boeche et al. 2011, SP_Ace Boeche & Grebel 2018), on-the-fly spectrum synthesis such as SME (Valenti & Piskunov 1996), on-the-fly flux ratios such as ATHOS (A Tool for HOMogenizing Stellar parameters, Hanke et al. 2018) or a comparison based on a synthetic spectra grid (FERRE Allende Prieto et al. 2006; MATISSE Recio-Blanco et al. 2006; GAUGUIN Bijaoui et al. 2012; Guiglion et al. 2016). These methods have shown their efficiency in deriving precise and accurate abundances for various spectral ranges and spectral resolutions in the context of the major current spectroscopic surveys, such as the Gaia-ESO Survey, APOGEE, GALAH, and RAVE. These families of standard pipelines are essential because they are based on the physics of stellar interiors, deriving atmospheric parameters and chemical abundances that can be used as stellar labels in the context of data-driven methods.

Indeed, data-driven approaches have started to play an important role in estimating these stellar labels. Such methods transfer the knowledge from a reference set of data, so-called training samples, to infer stellar labels.

The Cannon (Ness et al. 2015) is one of the pioneering data-driven analysis packages and its reliability was demonstrated through applications to spectroscopic surveys such as APOGEE and RAVE (Casey et al. 2016, 2017). The

Payne (Ting et al. 2019) recently demonstrated that one can couple stellar spectra modeling and a model-driven approach to reflect stellar labels. We note that the Cannon uses observed spectra (with the same set-up, but higher signal-to-noise (S/N) than the survey) as the training data while the Payne uses synthetic spectra as the training set.

A few recent studies used convolutional neural networks (CNNs) to infer atmospheric parameters and chemical abundances from high-resolution spectra. Leung & Bovy (2019) derived 22 stellar parameters and chemical abundances based on APOGEE DR14 spectra and labels, utilizing their astroNN tool and purely observational data. On the other hand, Fabbro et al. (2018) developed the StarNet pipeline, based on a CNN and an input synthetic spectra grid. They applied their StarNet to high-resolution data of APOGEE and more recently to Gaia-ESO Survey UVES spectra (Bialek et al. 2019). Zhang et al. (2019) used StarNet to estimate atmospheric parameters and chemical abundances of LAMOST spectra, based on APOGEE results.

The goal of the present paper is to show that a CNN-based approach can be employed for an efficient transfer of stellar labels from high resolution spectra to intermediate resolution spectra. This is done in conjunction with additional observables in the form of stellar magnitudes and parallaxes. We aim to derive atmospheric parameters and chemical abundances from intermediate-resolution RAVE DR6 spectra, based on a training sample of common stars with higher resolution APOGEE DR16 (Ahumada et al. 2019) spectra. We also show that using broad-band infrared photometry and parallax measurements as an extra set of constraints during the training phase improves the atmospheric parameters considerably. This study represents a complementary approach to the RAVE project's main parameter pipeline, and enhances the scientific output of the RAVE spectra. This work also has a good synergy with the next full Gaia release (Gaia DR3), which will provide spectra from the Radial Velocity Spectrometer (RVS), that are very similar to RAVE spectra in terms of wavelength coverage and resolution.

The paper is laid out as follows: in Sect. 2, we present the data used to build the training sample; in Sect. 3, we present the main features of the CNN and give details about the training phase; in Sect. 4 we deduce the atmospheric parameters and chemical abundances for more than 420 000 RAVE spectra, while the error budget is treated in Sect. 5. In Sect. 6 we compare and validate the tests with respect to external data sets. The scientific verification for some typical Galactic archaeology applications is presented in Sect. 8.

2. Training sample

One of the main goals of this study is to show that one can use high-resolution stellar labels to deduce atmospheric parameters and chemical abundances from lower-resolution spectra. For this purpose, we need to build a training set that contains the labels - the parameters we wish to derive (in our case atmospheric parameters and chemical abundances) and observables (the spectra and photometric measurements). We chose to work in this study with labels provided by the APOGEE survey and observables from the RAVE spectroscopic survey, complemented by 2MASS (Skrutskie et al. 2006), Gaia DR2 (Gaia Collaboration et al. 2018a), and ALL_WISE photometry (Wright et al. 2010)

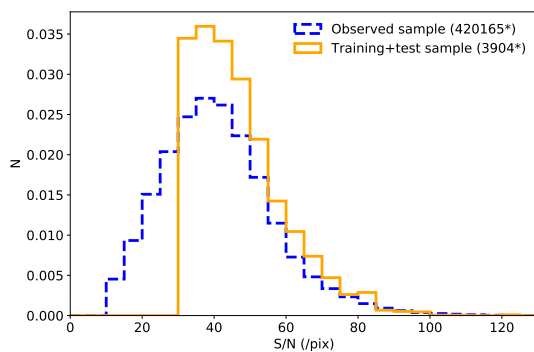


Fig. 1. Normalized distribution of signal-to-noise ratios (S/N) of RAVE DR6 spectra in the observed sample (blue dashed line, 420 165 stars) and in the training and test samples (solid orange line 3 904 stars in common between RAVE DR6 and APOGEE DR16).

and Gaia DR2 astrometry (Lindgren et al. 2018). Since the APOGEE survey, on average, offers higher resolution and higher signal-to-noise ratios (S/N) than the RAVE survey, we can translate the higher quality of the derived APOGEE labels to RAVE.

We take advantage of the latest release of APOGEE, the DR16 (Ahumada et al. 2019) providing high-quality atmospheric parameters and chemical abundances. APOGEE spectra are taken at near-infrared wavelengths with high resolution ($R = 22\,500$ and $\lambda \in [1.5 - 1.7]\mu\text{m}$).

The RAVE DR6 spectra have a spectral resolving power of $R \sim 7\,500$. We re-sampled the spectra to a common wavelength coverage of $\lambda \in [8\,420 - 8\,780]\text{\AA}$, with equally spaced 0.4\AA pixels.

We performed a cross-match based on the Gaia DR2 Source IDs between the 518 387 RAVE DR6 observations and the 473 307 observations of APOGEE DR16, resulting in a sample of $\sim 7\,000$ sources. In order to build a clean and coherent training sample based on APOGEE stellar labels and RAVE spectra, we cleaned this cross-matched sample in the following way:

- We required that a given star has available measurements of T_{eff} , $\log(g)$, $[M/H]$, $[Fe/H]$, $[\alpha/M]$, $[Mg/Fe]$, $[Si/Fe]$, $[Al/Fe]$, $[Ni/Fe]$ and their associated errors in the APOGEE set. We excluded parameters for stars with $S/N_{\text{APOGEE}} < 60$ (per pixel), and required that the ASPCAP¹ parameterization flag is `aspcap_flag=0`. The mean APOGEE S/N of the sample is 420 per pixel. We filtered stars with a bad flag on chemical abundances, *i.e.* only selecting `X_Fe_FLAG=0`.
- We adopted the normalized, radial-velocity-corrected spectra from the DR6 of RAVE. We required that the spectra have at least $S/N > 30$ per pixel. We excluded spectra showing signs of binarity or continuum issues ('c', 'b', and 'w' according to the RAVE DR6 classification scheme, see Steinmetz et al. 2020a).
- As detailed in Sect 3.2, we used absolute magnitudes during the training process. We required that a star has an apparent magnitude available in the 2MASS JHK_s , ALL_WISE W1&2 pass-bands, and Gaia DR2 G , G_{BP} , G_{RP} , and Gaia parallaxes (with parallax errors $e_p <$

15%). As such apparent magnitudes can suffer from dust extinction, we took advantage of the StarHorse catalog that provides improved extinction measurements based on RAVE and Gaia DR2 data (Queiroz et al. 2019, see also Santiago et al. 2016; Queiroz et al. 2018 for details on the method). We required that all spectra have an available StarHorse extinction (A_V).

The resulting common sample between APOGEE DR16 and RAVE DR6 consists of 3 904 high-quality RAVE spectra and high-quality atmospheric parameters and chemical abundances. The RAVE S/N distribution of this sample is presented in Fig. 1. We carefully checked the spectra of the 3 904 stars of the sample in order to reject any misclassified stars, possibly having a very low S/N . Some examples of RAVE spectra are presented in Fig. 2, for typical metal-poor and metal-rich dwarfs and giants. Kiel diagrams of the 3 904 targets based on APOGEE DR16 parameters are presented in the left panels of Fig. 7.

3. Training the network

An artificial neural network consists of several layers of neurons that are interconnected. The strength of connections between the neurons is governed by the weight of each connection. This feature enables the network to translate the input data vector to the desired output labels. The weights need to be set to values with which the translation becomes meaningful. For example, a stellar spectrum sampled at N wavelength points is fed into a neural network with N input neurons and the network produces an output in the form of, say, effective temperature. The setting of weights is done through training. This is a process of passing a limited set of data vectors through the network and gradually adjusting the weights so that the output matches the pre-determined labels of the data vectors. Each passing of the input data and adjustment of the weights is known as an epoch and many epochs are needed to successfully train the network. Once this is done, a new data vector can be passed through the network and we obtain its label as a result. We note that convergence is reached when the error from the model has been sufficiently minimized. In theory, it could happen that the desired level of error minimization is never reached and the network would run indefinitely. We detail in Sect. 3.3 how we stop the training.

3.1. Architecture of the CNN

In Fig. 3 we present the architecture of the neural network used in this study. It is composed of three convolutional layers and two fully-connected or dense layers. Below we justify the reason for utilizing these features. We used the Keras python libraries for coding the network (Chollet et al. 2015). The stellar labels are normalized, ranging from 0 to 1 by using a Min-max normalization.

3.1.1. The convolution and dense layers

Convolution layers are the key for detecting patterns and features in images (see for example Cireřan et al. 2011 for more details on this topic). In the present study, we work with one-dimensional normalized stellar spectra characterized by spectral line features. Such spectral features are indicators of the physical properties of the stars (temperature,

¹ APOGEE Stellar Parameter and Chemical Abundance Pipeline, García Pérez et al. 2016

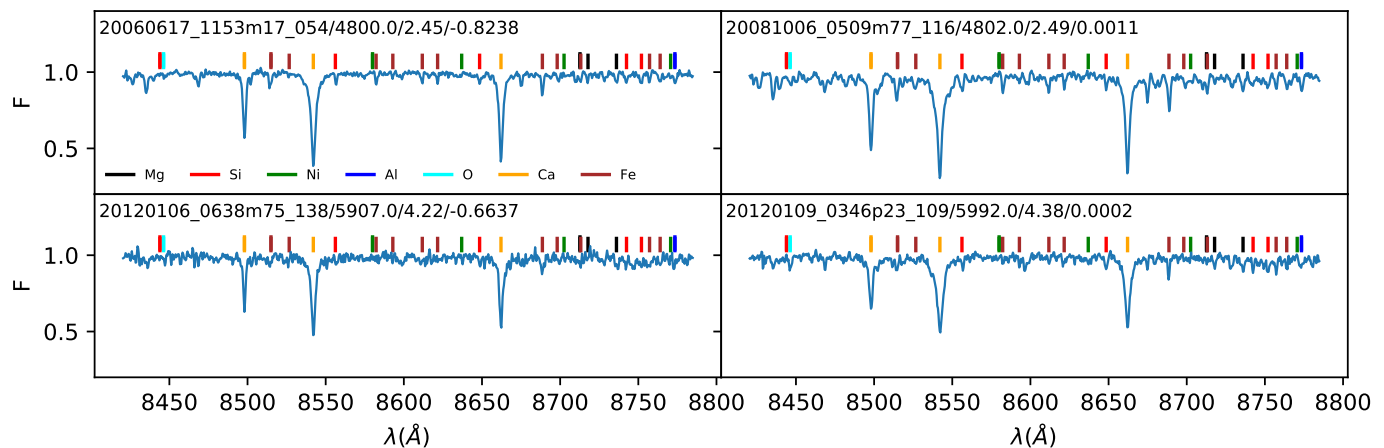


Fig. 2. Example of 4 typical metal-poor and metal-rich dwarfs and giants RAVE spectra from the training sample. The RAVE_OBS_IDs and the atmospheric parameters are indicated in the top left corner of each panel. Apart from the prominent CaII triplet lines, the RAVE spectra also show a variety of more subtle spectral features (main chemical abundance diagnostic lines are over-plotted).

gravity, chemical composition, etc). The ability to capture the relations between the different wavelength pixels in a spectrum, as opposed to treating them as independent entities, is the key to improved performance and is provided by the convolutional layers.

To understand the impact of these types of layers we experimented with training our network with and without the convolution stage. In comparison to the network with the convolution stage, the training phase to find a stable solution is three to four times longer for the non-convolutional network. In addition to lengthier training, the output parameters are not recovered as precisely. This applies in particular to chemical abundances. After trying many different layouts, we adopted a network with three convolution layers, containing eight, four, and two filters, respectively (as shown in Fig. 3). We adopted a kernel size of 10 pixels for all three layers. Tests revealed that kernel sizes between 5 to 20 pixels tend to extract features efficiently. Much larger kernels (>40 pixels) degrade the performance.²

Between the convolution layers and the fully-connected part of the network, we used a dropout layer that ensures a certain randomly chosen fraction of the neurons are not used at each of the epochs during the training phase. This type of regularization prevents over-fitting the network and prevents the algorithm from relying on a smaller part of the network alone. We tested a range of fractions from 10 to 30%, with no major change in the training phase. We adopted 20% for the final analysis.

The fully connected layers (also called 'dense' layers) following the convolutional stage are a more common type of neural network layers. They receive the output of the convolutional stage in the form of learned spectral features and convert them to the output labels (atmospheric parameters, abundances) that we desire. We must allow enough complexity in the network at this stage for it to be able to model the non-linear relations between features and labels.

² We note that the performance of the network is not impacted by a random uniform shift of a spectrum's continuum of up to 20% in flux. This implies that the network does not extract information from the overall level of the continuum.

3.1.2. Initializers and cost-function

The weights of the CNN need to be initialized before the training. The choice of how we initialize them can influence the performance of the network. We used uniform initialization for all the weights across the network, meaning that the weights before the training are drawn from a uniform distribution within a certain range.

To train the network we need a cost function that evaluates how good the network's performance is at each iteration and also allows us to compute the gradient in the weight space so the difference between the output and pre-determined labels can be minimized. The choice of this function is important. We experimented with a simple mean-squared error loss-function and a negative log-likelihood criterion. Tests performed on the negative log-likelihood criterion revealed that such a criterion appears to be inferior for our science case, and it adds too much complexity to the framework.

3.1.3. Effect of noise in the training phase

The training and test samples include in total 3904 stars with $S/N > 30$ per pixel. As a test, we constrained this range to $S/N > 40$ (2529 stars) and $S/N > 50$ (1289 stars). With a lower number of stars, the performance naturally tends to degrade. We believe, however, that this lack in performance is only due to the fact that we have a limited common sample with APOGEE. In general, high S/N data and sufficient statistics lead to a better training phase, but lower S/N spectra also come with a higher degree of correlated noise which the network likely learns about.

As another check, we extended the S/N range to $S/N > 20$, $S/N > 15$ and $S/N > 10$ per pixel, leading to 4802, 5023, and 5136 stars in the training sample. We concluded that including such low- S/N data in the training phase tends to reduce the quality of the training, and degrades the overall performance.

We tried to train a network with a sample composed only of stars with $S/N < 30$, finding that no robust solution could be reached, probably owing to the spectral information being too hidden by noise. Especially for the

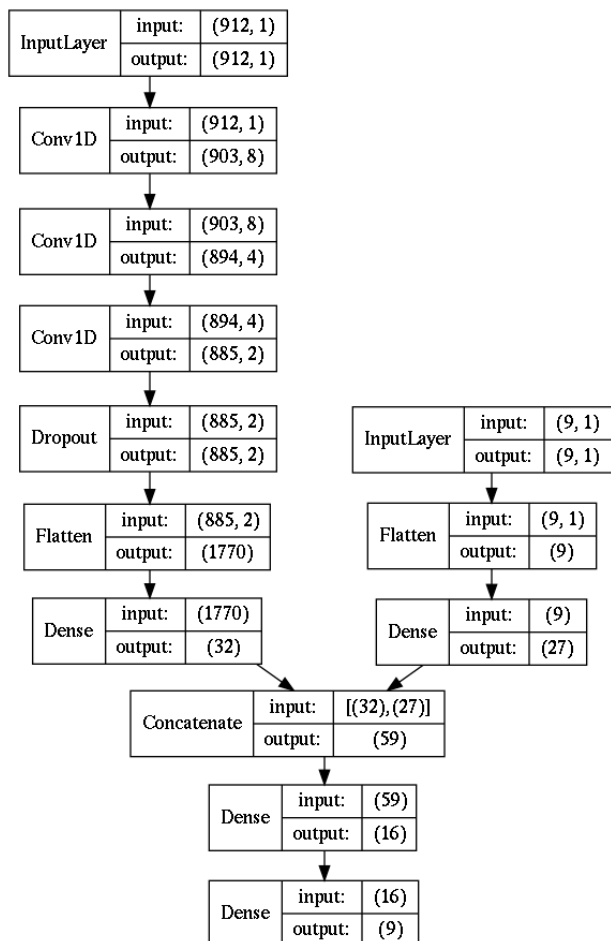


Fig. 3. Representation of the architecture of the Keras model used in this study. The input layer (the spectra) is passed through three steps of convolution (Conv1D). Then, we randomly drop 20% of the neurons at each epoch of training with the dropout layer in order to prevent overfitting. We then flatten the output for the next dense layer (also called fully connected layer). As an additional input, we include eight absolute magnitudes (2MASS JHK_s , ALL_WISE W1&2, and Gaia DR2 G , G_{BP} , G_{RP} passbands) and one A_V correction (input layer with shape of 9). We concatenate it to the main part of the network in the form of 27 neurons. The fully connected part of the network is then composed of two dense layers. The output is an array of nine parameters (atmospheric parameters and six chemical abundances).

chemical abundances, the network is unable to reproduce the main Galactic trends and basically fits a straight line in the $[\alpha/M]$ vs. $[M/H]$ plane instead of reproducing the α -rich and α -poor sequences. A similar finding also holds for other elements. Our conclusion is that an efficient training cannot be performed if only low- S/N stars are present in the training set.

We recommend that for future spectroscopic surveys particular attention should be given when defining the training sample S/N range, because too low- S/N spectra lead to worse training and performances of the CNN.

3.2. Feeding absolute magnitudes to the neural network

In addition to spectra as our input we included broad-band photometry. Absolute magnitudes provide strong con-

straints on the effective temperature and the surface gravity of a star. We adopted the 2MASS apparent magnitudes m in the passbands JHK_s (1.235, 1.662, and 2.159 μm , respectively), ALL_WISE W1 and W2 pass-bands (3.4, and 4.6 μm) and Gaia DR2 G_{BP} (328.3-671.4 nm), G_{RP} (629.6-1063.7 nm) and G (332.1-1051.5 nm) bands, using the cross-matches provided in RAVE DR6 (Steinmetz et al. 2020a). The distributions of these apparent magnitudes are shown in Fig. 4.

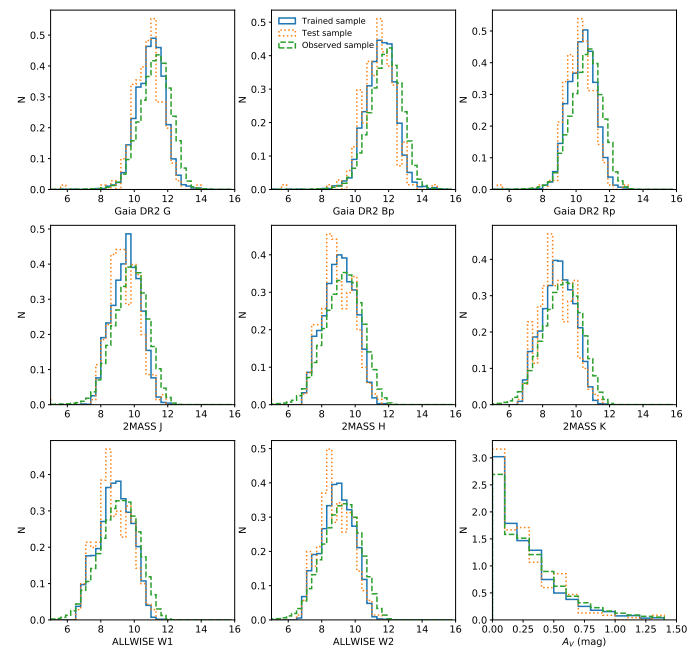


Fig. 4. Normalized distribution of Gaia, 2MASS, ALL_WISE apparent magnitudes and extinction (A_V) for the training sample (blue, solid), the test sample (orange, dotted) and the observed sample (green, dashed). Those magnitudes are converted to absolute magnitudes and are used during the training phase.

We computed absolute magnitudes M using the parallaxes (p) from the second data release of the Gaia satellite (Gaia Collaboration et al. 2018b), using $M = m + 5 \times [\log_{10}(p) + 1]$. We selected the best measurements for which we required the errors on the parallax, e_p , to be better than 20% (96.5% of the spectra of the initial cross-match with APOGEE DR16 fulfill this criterion).

As stellar magnitudes can suffer from dust extinction even in the infrared passbands, we adopted the extinction correction A_V from StarHorse (see Queiroz et al. (2018); Anders et al. (2019) for more details). The distributions of A_V for the training, test, and observed sample are presented in Fig. 4. 78% of our stars have an extinction lower than $A_V = 0.5$ mag. Our tests found that stars with $A_V > 0.8$ show a smaller error in T_{eff} by 20 K if we include this correction.

Our choice to compute absolute magnitudes from parallaxes instead of, for example, StarHorse distances was motivated by the fact that we want to restrict our model dependency as much as possible. As a test, we computed absolute magnitudes using StarHorse distances, but no notable difference in the training was measured.

The eight absolute magnitudes and the extinction corrections are then added smoothly to the CNN architecture, directly in the fully connected part, as 27 neurons (see scheme in Fig. 3). We tested several layer sizes for this part:

below 27 the performances tended to degrade, and above 27, no further improvement was notable. We note that we did not directly apply the A_V correction to the absolute magnitudes, thus leaving the network with more flexibility to learn from it.

It has been shown that Gaia DR2 astrometric measurements have small systematic errors, in particular an offset of the parallax zero-point that varies across the sky. This parallax zero-point offset is dependent on magnitude and color (Lindgren et al. 2018; Arenou et al. 2018). This offset is roughly of the order of $50 \mu\text{as}$. Following the way we compute our absolute magnitudes, this parallax offset translates into a shift of the order of 0.01 magnitudes. In the context of this study, this offset is negligible.

We refer the reader to Sect. 7 for a discussion on the gain of adding photometry during the training process.

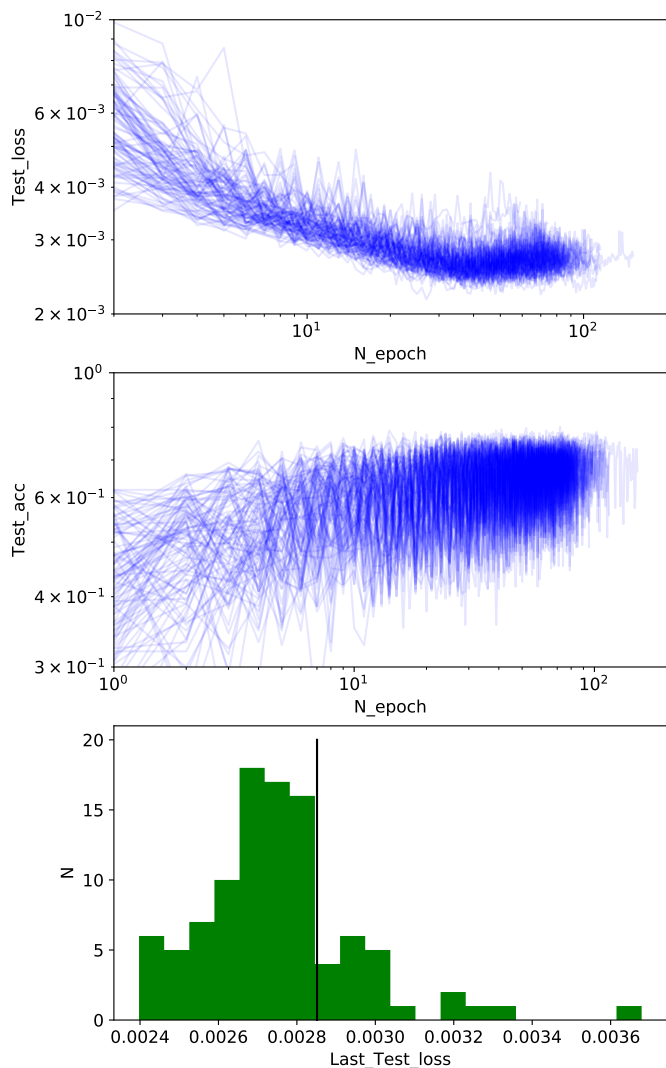


Fig. 5. Top panel: value of the cost function for the test sample (Test_loss) for the 100 CNN runs as a function of the epoch. Middle panel: accuracy computed on the test sample (Test_acc) as a function of the epoch. Bottom panel: distribution of 100 values of Test_loss after the training was completed. The vertical black line indicates the 80 percentile of the distribution.

3.3. Training an ensemble of 100 CNNs

From the quality cuts and selection process detailed above, our starting sample is composed of 3905 stars, with stellar labels corresponding to atmospheric parameters and chemical abundances.

Before training the CNN, we split the data into a training sample and a test sample, as is a common practice in the machine-learning community. We adopted a fraction of 6% for the test sample, in order to retain a large the training sample. This led to 3669 stars in the training sample and 235 stars in the test sample. We tested several test/training fractions, from 3 to 40%, with no major difference in terms of training.

In order to provide stable results and errors, we built an ensemble of 100 trained CNNs, all of them initialized differently. A similar method was recently used by Bialek et al. (2019).

One challenge while using a CNN is to stop the learning phase at the right time. The model can under-fit the training and test samples in case of insufficient training. On the other hand, in case of over-fitting, the training sample will perfectly fit the model, but the performances on the test sample will degrade drastically (which is the main reason behind the training-test split). One solution is to stop the training phase when the performance on a validation dataset starts to degrade. In this context, we adopted the commonly used early-stop procedure. If after 40 epochs (the so called patience period) the solution did not improve we stopped the training. We tried different levels of patience, finding that 40 epochs provide the best compromise between final accuracy and computation time.

Typical curves of the cost functions ' Test_loss ' for the test sample are presented in Fig. 5 for the 100 runs, as well as the accuracy Test_acc . One can see that the training phase takes no more than 120 epochs. Training the CNN takes between 70 to 90 seconds per run. One can also see that the last value of the cost function of the test sample (Last_Test_loss) can vary from one run to another. We plot such values in the bottom panel of Fig. 5. We excluded networks with too large a value of Last_Test_loss (everything inside of the lower 20th percentile of the distribution).

3.4. Result of the training

In Fig. 6 we compare the labels used as input of our CNN to those trained by the network (averaged over the 80 runs). The network is able to learn a significant amount of information about the main atmospheric parameters T_{eff} , $\log(g)$, $[\text{M}/\text{H}]$ as well as $[\text{Fe}/\text{H}]$. No obvious systematic trends are visible while the dispersion is low, for both training and test samples. Abundances $[\alpha/\text{M}]$, $[\text{Si}/\text{Fe}]$, $[\text{Mg}/\text{Fe}]$, $[\text{Al}/\text{Fe}]$ and $[\text{Ni}/\text{Fe}]$ compare well with the input labels. Because of poor mapping of the parameter space, the stars with very low or very high abundance ratios can suffer from systematic trends, especially in the metal-poor regime. In general, the dispersion in the test sample is similar to the one in the training sample, indicating that we do not over-fit our data. We finally note that for $[\text{Al}/\text{Fe}]$ and $[\text{Ni}/\text{Fe}]$, the comparison with the input APOGEE DR16 labels does not track the 1-to-1 relation, even for the bulk of the data, meaning that the model predicted during the training could suffer from systematic trends for those two elements.

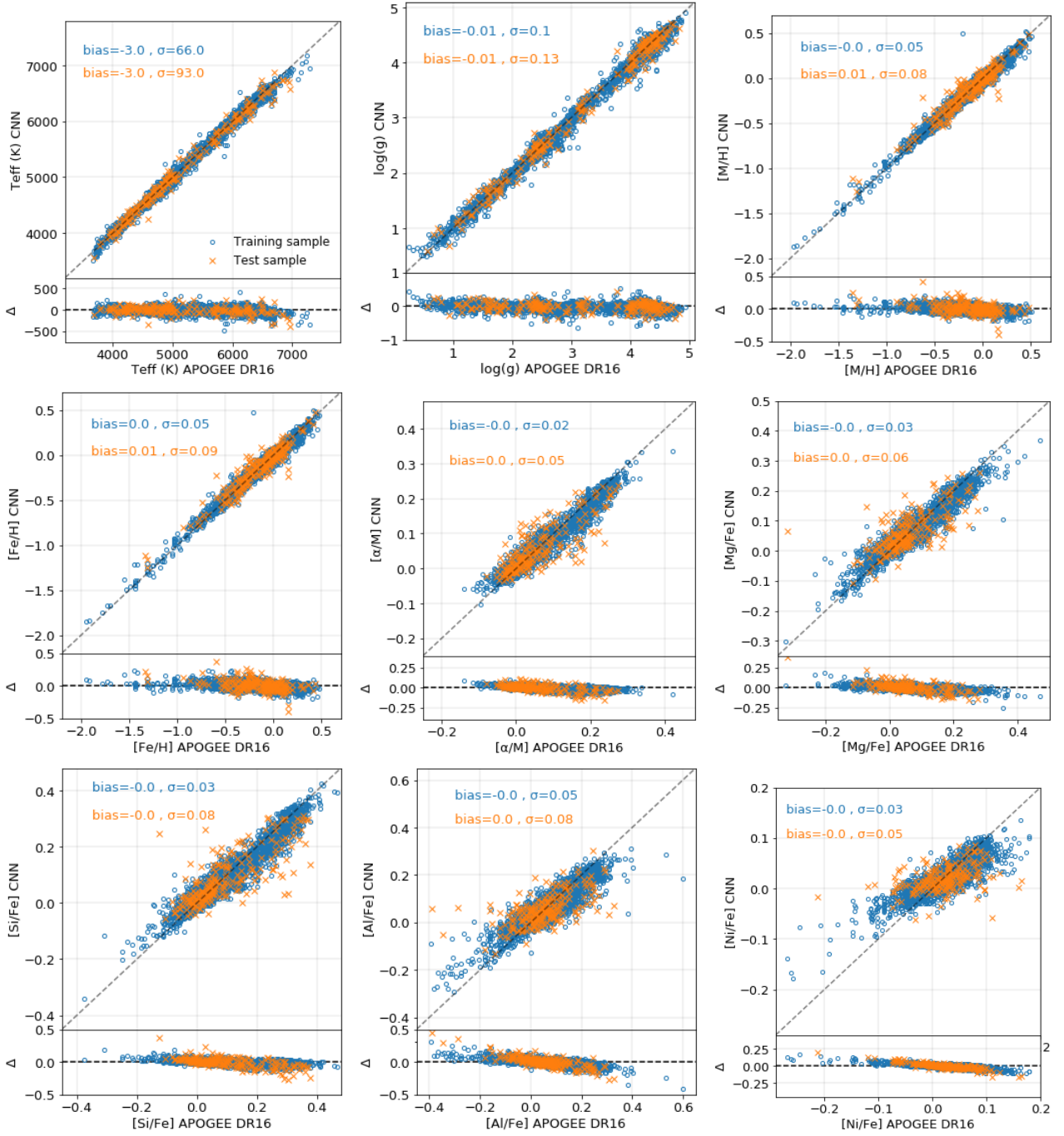


Fig. 6. One-to-one relation between the CNN trained labels (y-axis) and the input labels (x-axis, APOGEE DR16 data). The training sample is plotted with blue circles, while the test sample is shown with orange crosses. For each parameter, the typical mean difference and scatter are computed in both sets. We plotted too the difference Δ between the CNN trained labels and the APOGEE DR16 input labels with the same symbols and colors

In Fig. 7, we present a Kiel diagram of T_{eff} and $\log(g)$ from the training sample (left columns), for the training (top) and test (bottom) samples. In the right columns, we present the labels as trained by the CNN. The main features in the Kiel diagram are well recovered in both training and test samples: the position and inclination of the red clump, the giant branch with a smooth metallicity sequence, the turn-off sequence. The sequence of the very cool dwarfs spans a large T_{eff} range, and shows low scatter even in the very cool regime.

In the left panels of Fig. 8, we present the abundance patterns used as input for our CNN, for both training and test samples. We recall that those labels ($[Fe/H]$, $[\alpha/M]$, $[Si/Fe]$, $[Mg/Fe]$, $[Al/Fe]$, $[Ni/Fe]$) are derived by APOGEE DR16. In the right panels, we present the labels as trained by our CNN, averaged over 80 runs. The chemical patterns of the trained labels, in particular $[Al/Fe]$, show slightly less scatter than the original labels (around 0.05 dex). This effect comes mainly from the fact that during the training, the neural network values tend to stay within the boundaries of the data. In spite of the poor mapping of the pa-

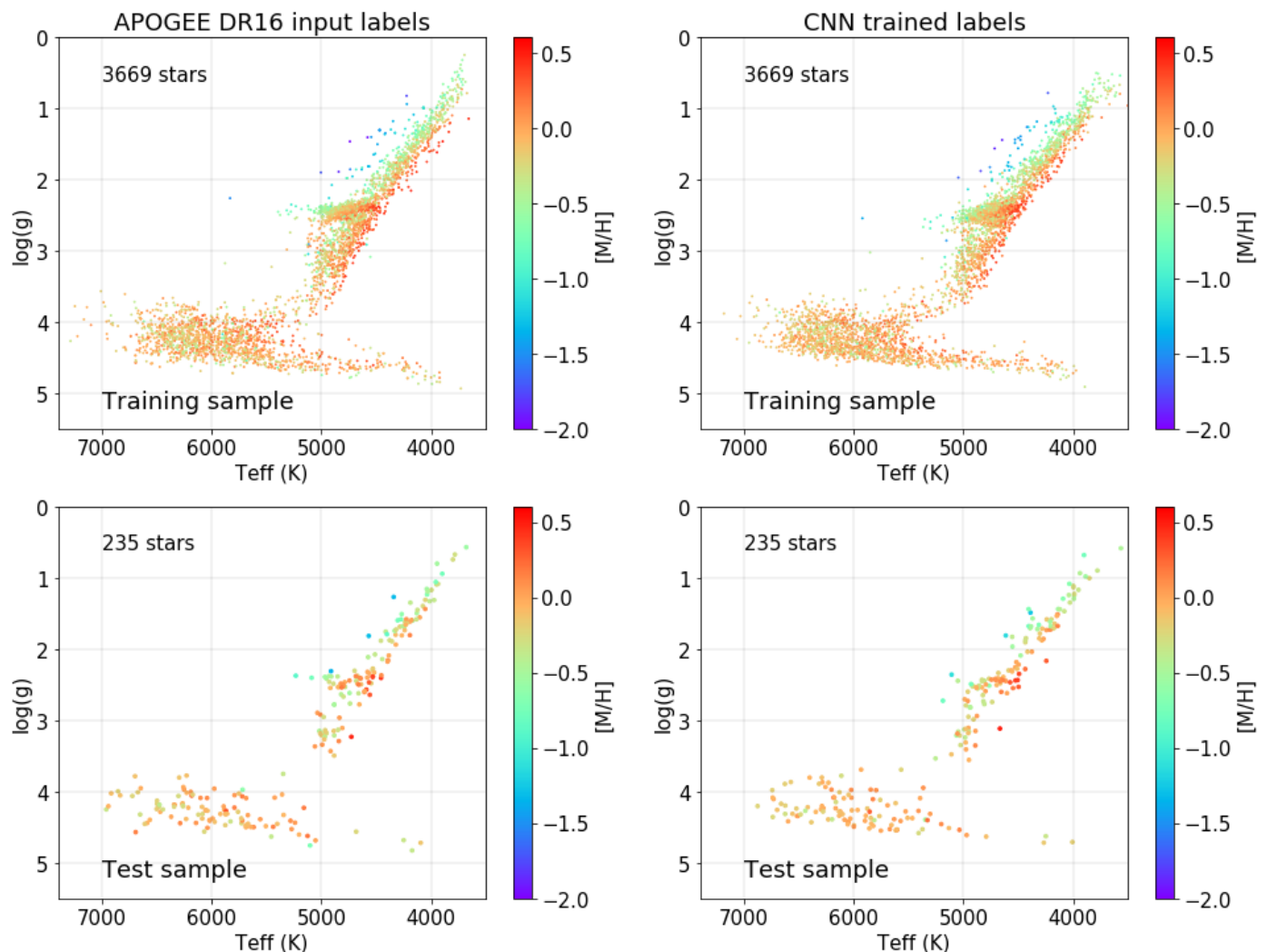


Fig. 7. Top left: Kiel diagram of the APOGEE DR16 stars (used in the training sample), color-coded with overall $[M/H]$. Top right: for the same stars, trained labels, averaged over 80 trained CNN. Bottom left: APOGEE DR16 parameters of the test sample. Bottom right: trained labels, averaged over 80 trained CNN, for the same test sample. The right panels correspond to what the network learns from the APOGEE parameters (left panels). The main features of the Kiel diagram are well recovered in both training and test samples, showing the robustness of the method.

parameter space in the metal-poor regime, the network is still able to provide robust output in that metallicity regime.

In Fig. 9, we present the averaged $[\alpha/M]$ ratios of the training sample, as a function of $[M/H]$, for different bins of T_{eff} and $\log(g)$. One can see that the $[\alpha/M]$ -rich sequence is mainly composed of red giant branch stars, while only a few stars are dwarfs. Similar plots are presented in Appendix A for $[Mg/Fe]$, $[Si/Fe]$, $[Al/Fe]$, and $[Ni/Fe]$.

4. Estimation of atmospheric parameters and abundances of RAVE DR6 spectra

In this section, we give details of the way we built an observed sample of stars based on RAVE DR6 spectra, then we present the predicted atmospheric parameters and chemical abundances of this observed sample.

4.1. Creation of the observed sample

Our observed sample is based on RAVE DR6 normalized radial-velocity-corrected spectra (Steinmetz et al. 2020a).

We required that a spectrum has ALL_WISE W1&2, 2MASS JHK_s photometry and Gaia DR2 G , G_{BP} , G_{RP} bands available as well as its Gaia DR2 parallax (no cut on parallax errors). We checked that all spectra have StarHorse extinction measurements (A_V , Queiroz et al. 2019). We finally restrained our observed sample to a range of $S/N > 10$ per pixel (as determined by RAVE DR6), removing stars with problematic spectra ("c" and "w" according to the RAVE DR6 classification). This leads to an observed sample composed of 420 165 stars with $S/N > 10$ per pixel. The S/N distribution of the observed sample is presented in Fig. 1.

Adopting the orbital data from Steinmetz et al. (2020b), we carefully checked that both the training and observed samples probe the same Galactic volume, in terms of mean Galactocentric radii and height above the Galactic plane. Also, as the stellar age distribution can vary from one sample to another we took advantage of the StarHorse ages of Queiroz et al. (2019) to check the age distributions of both the training and observed samples. The age distributions cover the same range and their shapes are consistent. Tests

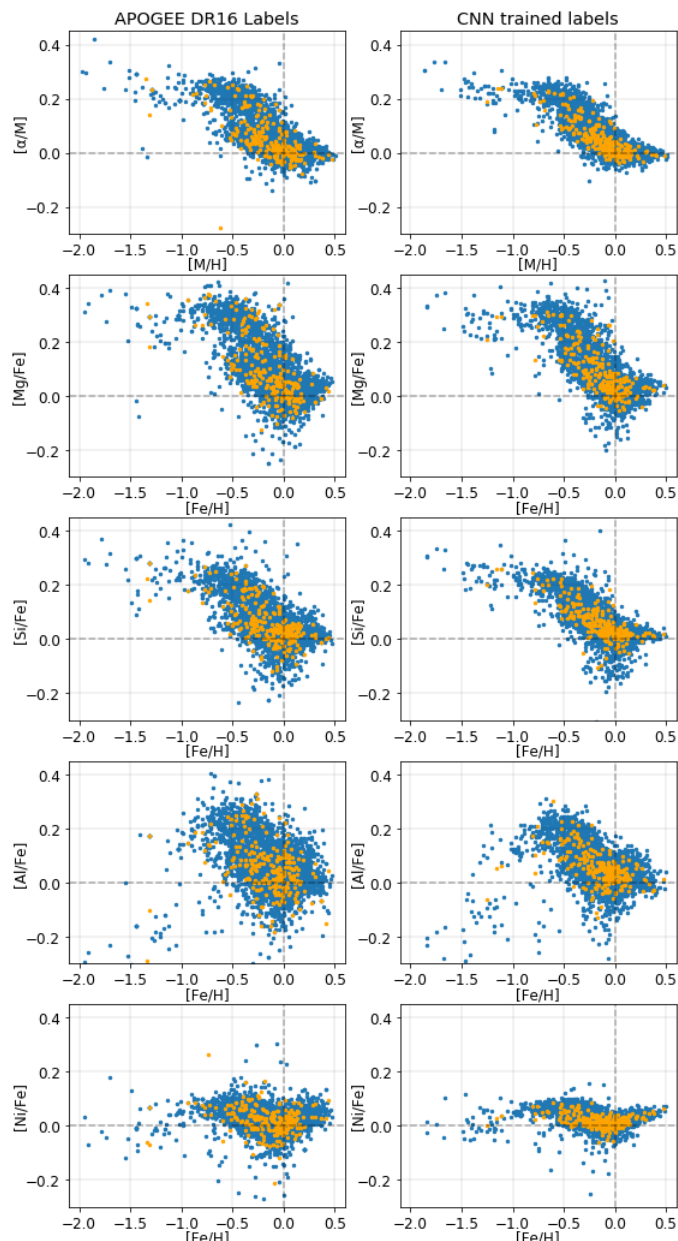


Fig. 8. Left panels: abundance patterns of the APOGEE DR16 labels used as input for our CNN, for the training sample (blue) and for the test sample (orange). Right panels: abundance patterns of the averaged labels trained over 80 CNNs.

performed with BDASP ages from Steinmetz et al. (2020b) led to the same conclusion.

4.2. Prediction of atmospheric parameters and abundances

Once a given CNN is trained we can predict atmospheric parameters and chemical abundances of the entire observed sample. Predicting nine parameters for 420 165 stars is fast, 10 seconds on a simple GPU unit. Then, estimating parameters for 80 CNN runs does not take more than 15 minutes. We then computed a set of parameters averaged over the 80 runs, as well a typical dispersion used as error (see Sect. 5).

4.2.1. Atmospheric parameters

In Fig. 10, we present a Kiel diagram of the observed sample, sliced in S/N, for 371 967 stars with $S/N > 20$ per pixel, and parallax errors better than 20%. We plotted such a diagram in two different fashions: color-coded with overall metallicity, and normalized-density map. For such a plot, we selected normal and hot stars ("n" and "o") according to the RAVE DR6 classification scheme (Steinmetz et al. 2020a).

At low S/N, we recover the main features of a typical Kiel diagram, especially the cool main sequence and the location of the red clump. The bottom of the cool main sequence shows a gradient in metallicity, while the turn-off shows no clear gradient. For very high S/N, the cool dwarf sequence is very narrow, while the red giant branch shows a slight warp as in the training sample. At low temperature ($T_{\text{eff}} < 4300$ K), we are able to properly characterize giants and dwarfs, putting them on the right sequence, with no degeneracy observed.

4.2.2. Individual chemical abundances

In Fig. 11, we present abundance patterns of $[\alpha/M]$ as a function of the overall metallicity $[M/H]$. We selected 301 076 stars with $S/N > 30$ per pixel, RAVE DR6 'n&o' classification ('normal' and 'hot' stars) and parallax errors lower than 20%. In order to disentangle the different stellar classes, we decomposed our sample in bins of 500 K in T_{eff} , and 1 dex in $\log(g)$, and present the $[\alpha/M]$ vs. $[M/H]$ trends for different locations in the Kiel diagram (see Appendix A for similar plots with $[\text{Si/Fe}]$, $[\text{Mg/Fe}]$, $[\text{Al/Fe}]$, and $[\text{Ni/Fe}]$).

Dwarf stars exhibit typical low- $[\alpha/M]$ sequences, while giants populate both the low- $[\alpha/M]$ and high- $[\alpha/M]$ range up to halo chemistry. Red clump stars show a smooth transition from the low- to the high- $[\alpha/M]$ regime, with a strongly decreasing density. On the other hand, in the range of $4000 < T_{\text{eff}} < 4500$ K and $1 < \log(g) < 2$, the high- $[\alpha/M]$ regime is clearly marked by a continuum of stars from solar- α up to 0.25 dex. Such behaviour is also observed when plotting $[\text{Si/Fe}]$ and $[\text{Mg/Fe}]$ as a function of $[\text{Fe/H}]$ (see Appendix A).

We note that the low-metallicity high- $[\alpha/M]$ plateau shows different behaviors in different regions of the Kiel diagram. This is mainly driven by the fact that we only have a few stars for $[M/H] < -1$ dex in the training sample, showing quite different trends. For future machine-learning applications, one should put strong efforts on properly mapping the parameter space when creating a training sample. The case of $[\text{Al/Fe}]$ is discussed in Appendix A.

We have shown that using a CNN approach and high-resolution stellar labels, we are able to provide reliable $[\alpha/M]$ values, for more than 301 076 stars, thus extending the scientific output of RAVE spectra beyond RAVE DR6.

4.2.3. Effect of parallax errors on the atmospheric parameters determination

In the present study, 94% of the RAVE DR6 targets have good Gaia DR2 parallaxes, with an error better than 20%. Deriving absolute magnitudes from such parallaxes and apparent magnitudes is then safe, in the context of the present paper. This high success rate is, however, an imme-

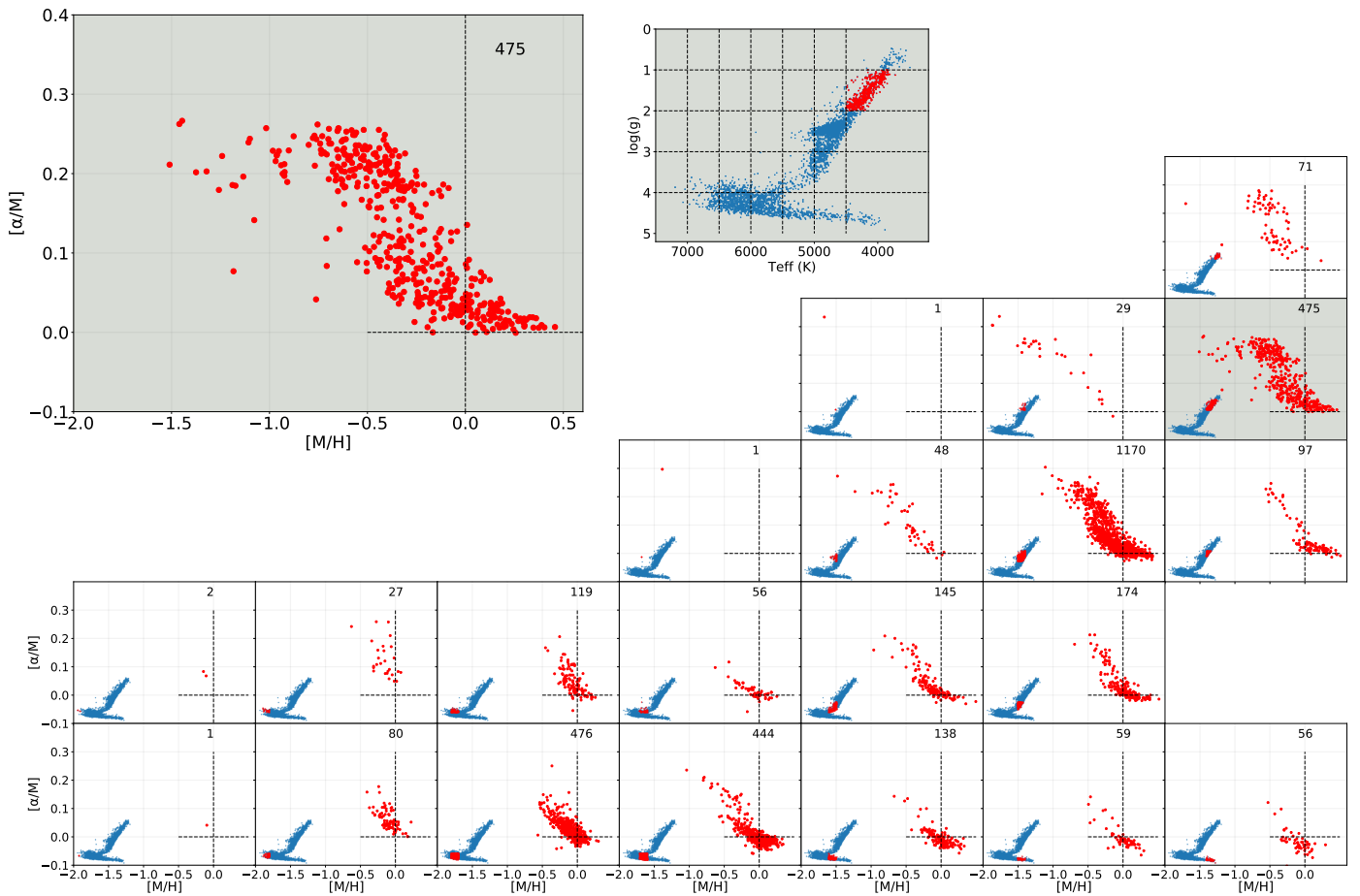


Fig. 9. Averaged trained abundance patterns $[\alpha/M]$ vs. $[M/H]$ for the training sample (red dots). Trends are shown for sub-samples in T_{eff} (500 K bins) and $\log(g)$ (1 dex bins) shown as in-set Kiel diagrams, where the overall stellar distribution is plotted in blue with the selected subsample highlighted in red. The number of stars is indicated in the top right corner of each panel.

diate consequence of the relatively bright magnitude limit of $I < 13$ for RAVE, with the majority of the stars even having $I < 12$. The overall Gaia RVS survey will, however, probe considerably fainter objects. The low-resolution surveys like Gaia RVS or 4MIDABLE-LR of 4MOST (Chiappini et al. 2019) will probe a much larger volume than RAVE. There is then a risk that many targets suffer from large parallax errors. We discuss here the impact of such large parallax errors on the determination of atmospheric parameters and abundances.

In Fig. 12, we present CNN results for 3502 stars of the observed sample with parallax errors $e_p > 20\%$, and $S/N > 50$ per pixel. Despite the large parallax errors, we can recover a proper giant branch with a clear metallicity sequence. Most of the stars with $e_p > 40\%$ are actually located in the upper part of either the main sequence or the cool giant branch. Such stars should be thus used with caution. For all stars with $e_p > 20\%$, the $[\alpha/M]$ vs. $[M/H]$ abundance patterns do not show systematics, meaning that chemical abundances are less sensitive to less precise parallaxes (absolute magnitudes constraining mainly T_{eff} and $\log(g)$).

To check if the CNN could learn from lower quality data, we added in our training sample ~ 150 more stars with parallax errors higher than 20%. Adding such stars did not improve the training phase or the atmospheric parameters

of the observed sample stars with parallax errors larger than 20%.

5. Determination of uncertainties

Despite the fact that we employ the same input labels in every run, the CNN does not provide the same trained labels, because a new set of weights is automatically generated by the CNN during each run and the trained labels then change slightly. We showed the resulting average trained labels in Sect 3.4. Here we present the resulting errors (precision), defined as the dispersion of each label for the 80 runs. As a result, the errors in both test and observed samples are derived in the same fashion. Normalized distributions of uncertainties are presented in Fig. 13 for atmospheric parameters and chemical abundances for 391 035 stars with $S/N > 20$ per pixel. Overall, the trained labels show on average smaller errors than the test and the observed sample, mostly because the training sample covers a higher S/N range. The test and observed sample tend to track each other well, meaning that we do not over-fit our model.

As a test, we added random offsets to the labels of the training sample, drawn from Gaussians with widths given by the quoted uncertainties from APOGEE DR16. We observed that the resulting error distributions barely change.

A recent study by Bialek et al. (2019) adopted a negative log-likelihood criterion instead of a mean squared error

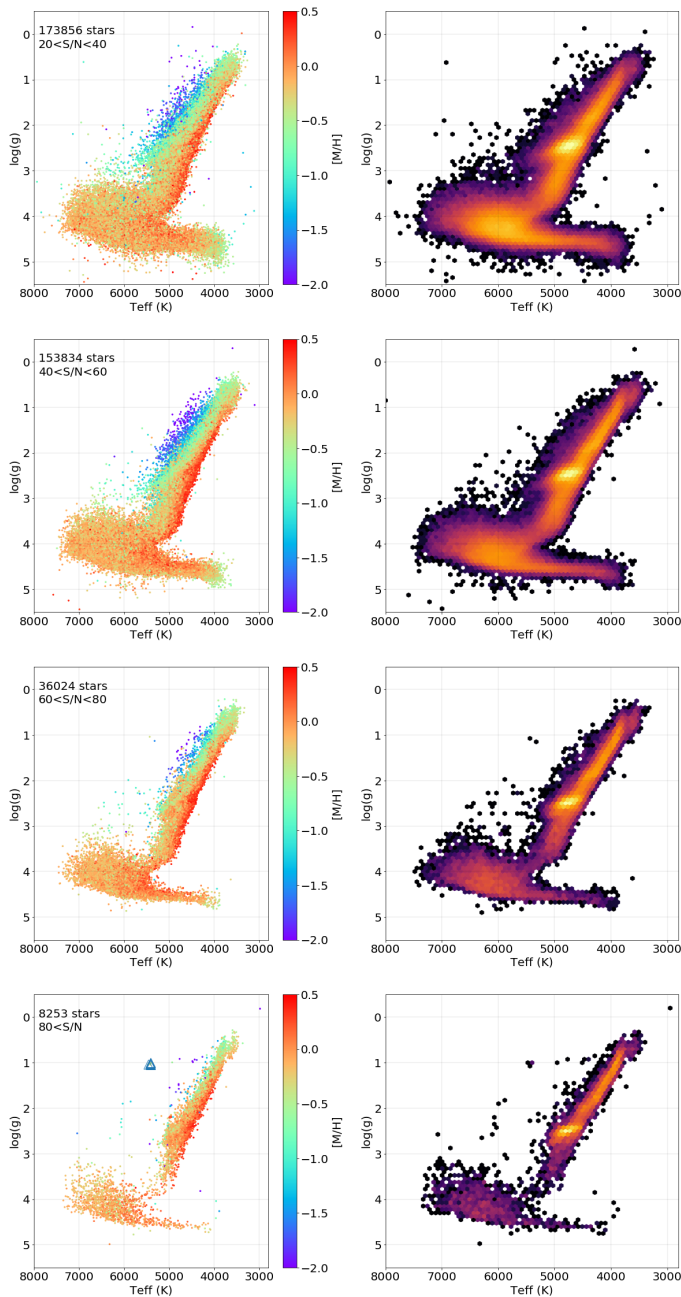


Fig. 10. Kiel diagram of 371 967 stars of the observed sample, sliced in S/N, color-coded by [M/H] (left column) and plotted as a normalized density map (right column). Only stars with "n" and "o" classification (normal and hot stars), and parallax errors better than 20% are plotted. The main features of the Kiel diagram are well recovered in the observed sample. The 6 blue triangles in the bottom panel correspond to the yellow supergiant Gaia "5983723702088571392", discussed in Section 6.8.

loss-function as employed in our study. In that way, they were able to derive the individuals error of the predicted atmospheric parameters. We explored such a criterion. Because it adds extra complexity to the framework and because of the limited number of stars in our training sample, this criterion did not provide improved results. We therefore kept a simple mean squared error loss-function, and errors derived over several CNN runs.

Machine-learning methods are, within limits, able to extrapolate and provide parametrizations for stars outside

the boundaries of the training sample parameter space. Together with individual uncertainties on the parameters and abundances, we provide individual flags for such stars. As an example, a star parametrized with an effective temperature inside the training sample space will have `flag_teff=0`, while the flag will be equal to 1 if T_{eff} is outside that range. Stars with flags equal to 1 may suffer from systematics caused by extrapolation outside the training sample parameter space.

6. Validation of atmospheric parameters and abundances

In this section, we proceed to several comparisons with respect to external datasets, in order to validate our atmospheric parameters and chemical abundances.

6.1. Validation of surface gravities with asteroseismic data

Asteroseismology of stars with solar-like oscillations is now widely used in large spectroscopic surveys as additional constraint, since it eventually calibrates the $\log(g)$ measured from spectra (RAVE: Valentini et al. 2017; GES: Pancino & Gaia-ESO Survey consortium 2012; APOGEE: Pinsonneault et al. 2018; LAMOST: Wang et al. 2016; GALAH: Kos et al. 2017). For stars with solar-like oscillations, as well as red giants, $\Delta\nu$, the frequency at maximum oscillation power, is used for determining $\log(g)_{\text{seismo}}$ using only the additional parameter T_{eff} . The $\log(g)_{\text{seismo}}$ value depends very weakly³ on T_{eff} , making this quantity reliable even for surveys affected by degeneracies such as RAVE (Kordopatis et al. 2011a, 2013).

The RAVE survey has some overlap with the fields observed by the K2 mission, the re-purposed Kepler satellite (Van Cleve et al. 2016). In Valentini et al. (2017), a first comparison (and consequent calibration) of the RAVE spectroscopic $\log(g)$ with the seismic value was performed using 89 targets in K2-Campaign 1. Information on the RAVE-K2 sample, the reduction of the seismic data, and the calculation of the seismic $\log(g)$ can be found in Valentini et al. (2017). In the first six Campaigns of K2, solar-like oscillations were detected for 462 red giants (Steinmetz et al. 2020b, Valentini et al, in prep.) and the seismic $\log(g)$ was derived. Here, we compare these seismic $\log(g)$ values with the values determined using our CNN.

Fig. 14 shows that the labels (APOGEE DR16) and the K2 $\log(g)$ values exhibit a tight and un-biased 1-to-1 relation (left panel, bias = -0.03 dex and dispersion $\sigma = 0.04$ dex).

The K2 $\log(g)$ values also compare well with the labels trained by the CNN (middle panel), with a slightly higher scatter ($\sigma = 0.09$ dex).

Finally, in the right panel of Fig. 14, we compare the predicted surface gravity for 433 common stars of our observed sample with K2 data, finding a very good agreement with a very small bias and a dispersion of 0.14 dex. We note that the $\log(g)$ values from RAVE DR6 show a larger scatter with respect to K2 data than our CNN $\log(g)$ values (see Figure 23 of Steinmetz et al. 2020a).

³ According to Morel & Miglio 2012, a shift of 100 K in T_{eff} changes $\log(g)_{\text{seismo}}$ only by 0.005 dex.

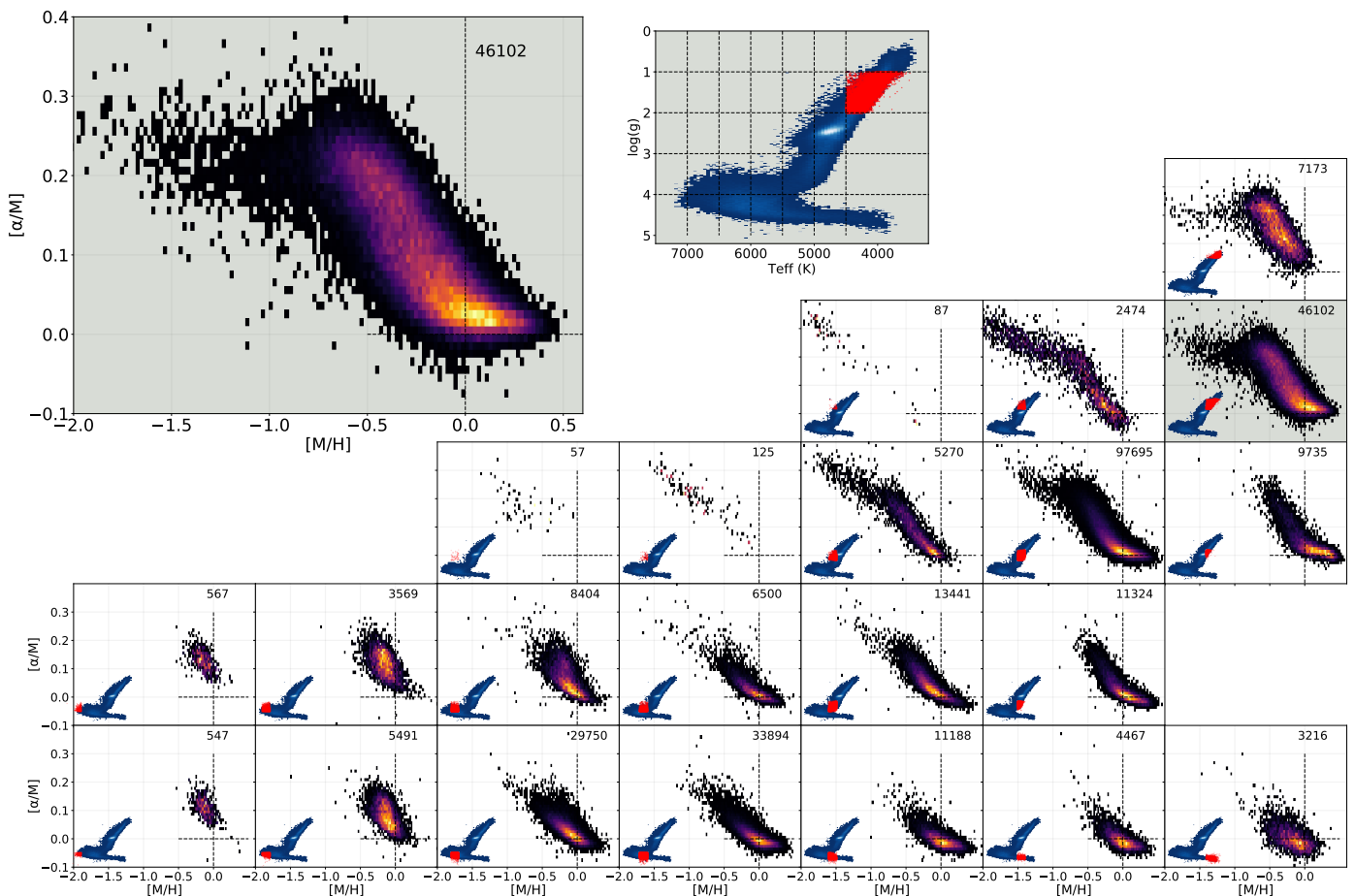


Fig. 11. $[\alpha/M]$ vs. $[M/H]$ for 301 076 stars of the observed sample with $S/N > 30$ per pixel, RAVE DR6 "n&o" classification, and parallax errors lower than 20%. The sample is presented in panels corresponding to cuts in effective temperature and surface gravity (steps of 500 K in T_{eff} and 1 dex in $\log(g)$). For each panel, we overplotted a $T_{\text{eff}} - \log(g)$ diagram with the location of the plotted stars marked in red.

Keeping in mind that we are limited by the narrow spectral range of the RAVE spectra, those comparisons illustrate all the potential of a method based on CNN.

A discussion on the impact of the use of photometry can be found in Sect. 7.

6.2. Comparison with RAVE DR6 BDASP $\log(g)$

In the latest data release of RAVE (DR6, Steinmetz et al. 2020b), improved $\log(g)$ estimates based on Gaia DR2 parallaxes and Bayesian isochrone fitting are provided, thanks to the BDASP pipeline (McMillan et al. 2018). This section is dedicated to comparing RAVE/BDASP surface gravities to those derived by our CNN in the present study.

The left panel of Fig. 15 compares the input APOGEE DR16 $\log(g)$ with those of BDASP. The dwarfs ($\log(g) > 3.5$) show a shift of about +0.1 dex, while the giants do not show any bias with respect to RAVE DR6. The typical dispersion is 0.14 dex for both types of stars with a bias of 0.05 dex. We notice that the surface gravities provided by APOGEE DR16 show a smaller dispersion around the red clump, compared to RAVE DR6, hence the presence of a diagonal line at $\log(g) \sim 2.5$.

Concerning the labels trained by our CNN, the bias decreases slightly (+0.04 dex), while the scatter drops to 0.09 dex. This decrease in the scatter is directly due to the fact

that we use absolute magnitudes during the training process, leading to more precise $\log(g)$ values (see Sect. 7 for more details). If no absolute magnitudes are used during the training phase, the scatter doubles to 0.17.

Finally, in the right column of Fig. 15 we compare the surface gravities predicted for 388 299 stars of the observed sample ($S/N > 20$) with respect to RAVE DR6. Again, the biases for giants and dwarfs keep the same shape as in the previous comparisons, and the scatter tends to still be quite low (0.12 dex). We notice that the scatter σ increases to 0.37 dex when no photometry is used in the training phase. A discussion on the impact of the use of photometry can be found in Sect. 7.

As a last note, we remind the reader that the input T_{eff} of the BDASP pipeline is the InfraRed Flux Method T_{eff} (see Steinmetz et al. (2020b) for more details). The BDASP T_{eff} tends to be very similar to this input. We explicitly compare our T_{eff} to T_{eff} IRFM in the next section.

6.3. Validation of effective temperatures with IRFM temperatures

A data product of the 6th data release of RAVE is the effective temperature derived via to the Infrared Flux Method (IRFM, Casagrande et al. 2006, 2010, see Steinmetz et al. 2020b for more details). In this section, we compare our ef-

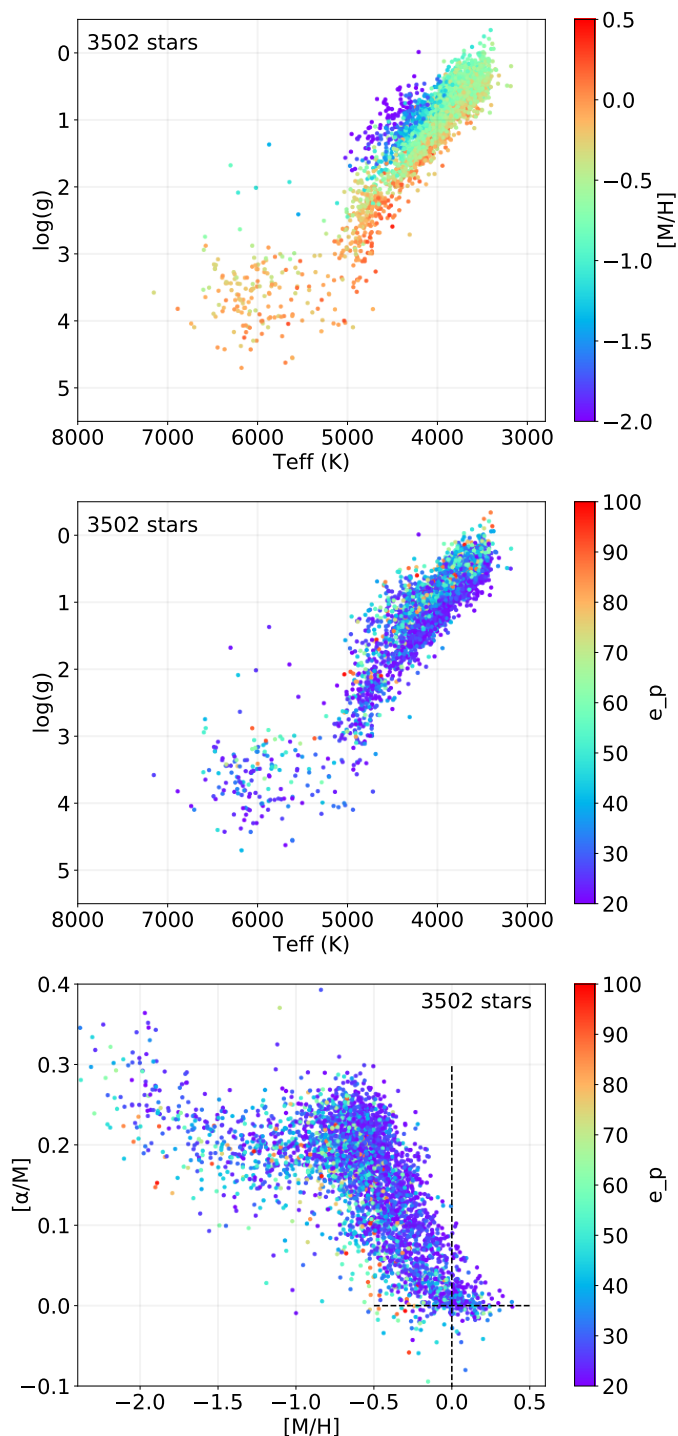


Fig. 12. Kiel diagram of 3 502 stars of the observed sample, with $e_p > 20\%$, color-coded by $[M/H]$ (top panel) and e_p (middle panel). Only stars with $S/N > 50$ per pixel are plotted. The same stars are presented in the bottom panels in the $[\alpha/M]$ vs. $[M/H]$ plane, color-coded by parallax errors.

effective temperatures to those provided by RAVE DR6. We compared the T_{eff} used in the training sample (APOGEE DR16 T_{eff}), those learned by the network, and those derived for the observed sample (for $S/N > 20$).

The results are presented in Fig. 16. We first see that there is a shift between the effective temperatures used as labels in our study and those of Steinmetz et al. (2020b) for hot stars ($T_{\text{eff}} > 5\,200\text{ K}$) which are offset by -250 K (con-

stant with temperature, with 260 K scatter). Those stars are mainly dwarfs. On the other hand, the cool stars of the training sample ($T_{\text{eff}} < 5\,200\text{ K}$, mostly giants) show a tight and un-biased 1-to-1 relation with respect to the IRFM temperatures (mean difference of -20 K and dispersion of 90 K). Overall, the dispersion is about 220 K for the 3651 stars of the training sample.

We note that stars with $T_{\text{eff}} > 5\,200\text{ K}$ tend to be cooler by 250 K with respect to the IRFM T_{eff} . The $\log(g)$ of such stars will be then systematically higher. This could be an explanation of the higher $\log(g)$ measured by our CNN with respect to BDASP $\log(g)$ (see previous section, Fig. 15).

Once the CNN is trained, the effective temperatures still show the same behaviour with respect to the IRFM T_{eff} .

Finally, one can see that the measured T_{eff} in 371 166 stars of the observed sample match in the same way the RAVE IRFM T_{eff} , with a larger scatter than the training sample mainly due to the presence of stars with lower S/N .

Overall, the effective temperatures used in the training sample (from APOGEE DR16), those trained, and those predicted agree pretty well with the T_{eff} IRFM from Steinmetz et al. (2020b). We finally note that this comparison basically only provides an assessment of the biases and scatter with respect to APOGEE DR16.

6.4. Validation of atmospheric parameters and chemical abundances with the HR sample

We compare here our atmospheric parameters and chemical abundances with those from high-resolution (HR) studies in the literature. We took a high resolution sample compiled and used for validation purposes in RAVE DR6 (Steinmetz et al. 2020b). It included more than 1700 stars, taken from several studies, among them with available chemical abundances Reddy et al. (2003); Valenti & Fischer (2005); Soubiran & Girard (2005); Reddy et al. (2006); Ruchti et al. (2011); Adibekyan et al. (2012); Bensby et al. (2014) and Gaia-ESO Survey DR5.

We present a Kiel diagram and abundance patterns for stars of the high-resolution sample and from the present study in Fig. 17. We only selected stars with $S/N > 20$. Basically, the main and giant sequences match pretty well. The $[\alpha/M]$, $[\text{Si}/\text{Fe}]$ patterns tend to match for $[\text{Fe}/\text{H}] > -0.5\text{ dex}$, while at lower metallicity the CNN abundances tend to be systematically lower. This comes from the fact that $[\alpha/M]$ and $[\text{Si}/\text{Fe}]$ do not reach values higher than $+0.30\text{ dex}$ in APOGEE DR16. On the other hand, $[\text{Mg}/\text{Fe}]$ matches pretty well between our CNN results and the literature. The $[\text{Al}/\text{Fe}]$ ratios are reasonably consistent around solar $[\text{Fe}/\text{H}]$, but the scatter increases for the metal-poor regime. Finally $[\text{Ni}/\text{Fe}]$ is rather flat in both samples, as expected for an Fe-peak element.

In Fig. 18, we present the 1-to-1 relations between the high-resolution sample and the present study. This illustrates very well the differences in the trends and zero-points. The typical dispersion is about 200 K in T_{eff} (no bias), while it is around 0.3 for $\log(g)$ (bias of 0.13 dex) and $[\text{Fe}/\text{H}]$ ($\sim 0.3\text{ bias}$). We observe an increase of the scatter with decreasing $[\text{Fe}/\text{H}]$. We note that the overall scatter in $[\text{Fe}/\text{H}]$ drops to 0.2 dex if we only select stars with $S/N > 50$. All other abundances show quite a small dispersion, roughly 0.1 dex . In fact, shifts in the trends or in the zero-points reflect more a systematic difference of the calibration between the APOGEE DR16 surveys and

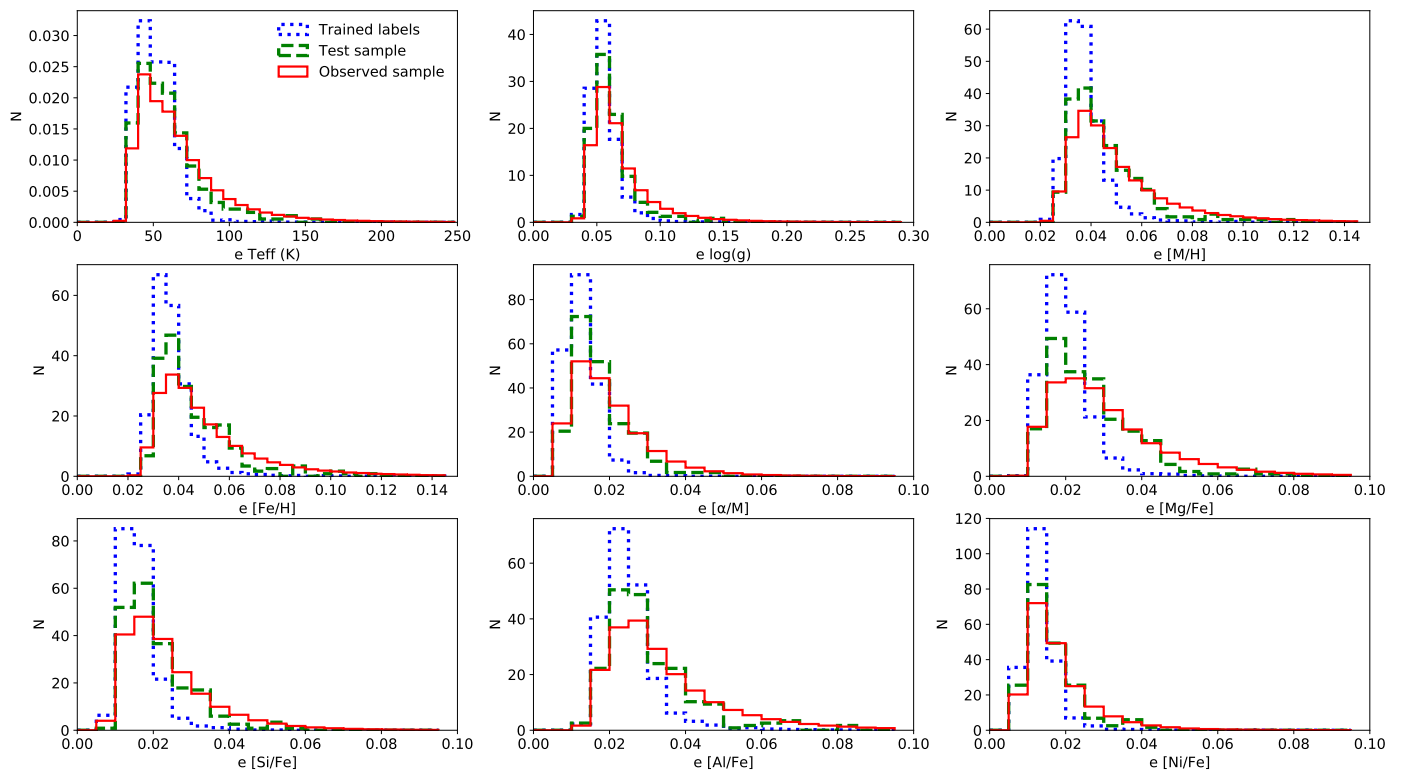


Fig. 13. Normalized distribution of errors of the atmospheric parameters and chemical abundances of the trained labels (blue, dotted), the test sample (green, long-dashed), and the observed sample (red, solid).

the test sample, rather than an incorrect estimation of parameters or abundances. Such differences are to be expected considering the differences in instrument specifications, resolution, wavelength range, and wavelength coverage.

6.5. Validation with repeat observations

Another way to show the reliability of our atmospheric parameters and chemical abundances is to investigate stars with repeated observations. We follow the same procedure as in Steinmetz et al. (2020a,b). Briefly, for a given star with several observations, we computed the differences in atmospheric parameters and chemical abundances. For all stars with multiple repeats, we analyzed the distribution of those differences. We approximated the distribution function by a combination of two Gaussians using a least-squares fit. The results are presented in Fig. 19, for all repeats (80 342 stars, $S/N > 20$). First, one can see that the distributions are roughly similar in shape for T_{eff} , $\log(g)$, $[M/H]$, and $[Fe/H]$. On the other hand, the chemical abundances of $[\alpha/M]$, $[Mg/Fe]$, $[Si/Fe]$, $[Al/Fe]$, and $[Ni/Fe]$ present asymmetric tails. The typical dispersion of the distribution for the effective temperature is about ~ 50 K, while for the surface gravity, the dispersion is below 0.05 dex. The dispersion increases to 80 K for T_{eff} and 0.14 dex for $\log(g)$ if we do not use photometry as extra information. For $[M/H]$ and $[Fe/H]$, the typical dispersion over all repeats is of the order of 0.05 dex. Finally, for $[\alpha/M]$, $[Mg/Fe]$, $[Si/Fe]$, $[Al/Fe]$, and $[Ni/Fe]$, a dispersion of 0.02-0.03 dex is measured over all repeats. These results imply that the CNN is precise (low dispersion within repeats) and accurate (overall difference distributions centered on zero) in determining atmospheric parameters and chemical abundances of RAVE spectra.

6.6. Validation with stellar clusters

In this section we compare the CNN results with 41 stars from 4 clusters used in RAVE DR6 for calibration purposes: 47Tuc (Carretta et al. 2009), Pleiades (Funayama et al. 2009), Blanco1 (Ford et al. 2005), IC4651 (Pasquini et al. 2004), Omega Centauri (Johnson & Pilachowski 2010). The results are presented in Fig. 20.

The giants tend to match pretty well between our study and the literature, with small variation from cluster to cluster. The Pleiades show no discernible offset in $\log(g)$ and $[Fe/H]$ while a large mean difference is measured for T_{eff} (-353 K). We have both giant and dwarf stars in common with IC4651, and they tend to show a good match with our study. The dispersion in $[Fe/H]$ drops to 0.03 when only considering stars with $S/N > 40$. We only have one star in common with Blanco 1, but we find good agreement between the literature and our study. Finally, the cluster 47Tuc presents an offset of $+0.13$ dex in $[Fe/H]$ with respect to the literature, while the dispersion is about 0.1 dex. We note that we have a total of 13 stars from 47Tuc and the Pleiades in our training sample. We have 12 giants in common with the metal-poor globular cluster Omega Centauri. The $[Fe/H]$ values of our CNN do not show any bias with respect to the literature, and the dispersion is about 0.1 dex. The Omega Centauri stars span lower $\log(g)$ values than 47Tuc, mainly $\log(g) < 1$. We show that the CNN is able to provide reliable parameterization of metal-poor super-giant stars.

The systematics observed in the 3 parameters directly come from systematics in the APOGEE DR16 labels. Overall, the typical dispersion σ in T_{eff} and $[Fe/H]$ tends to

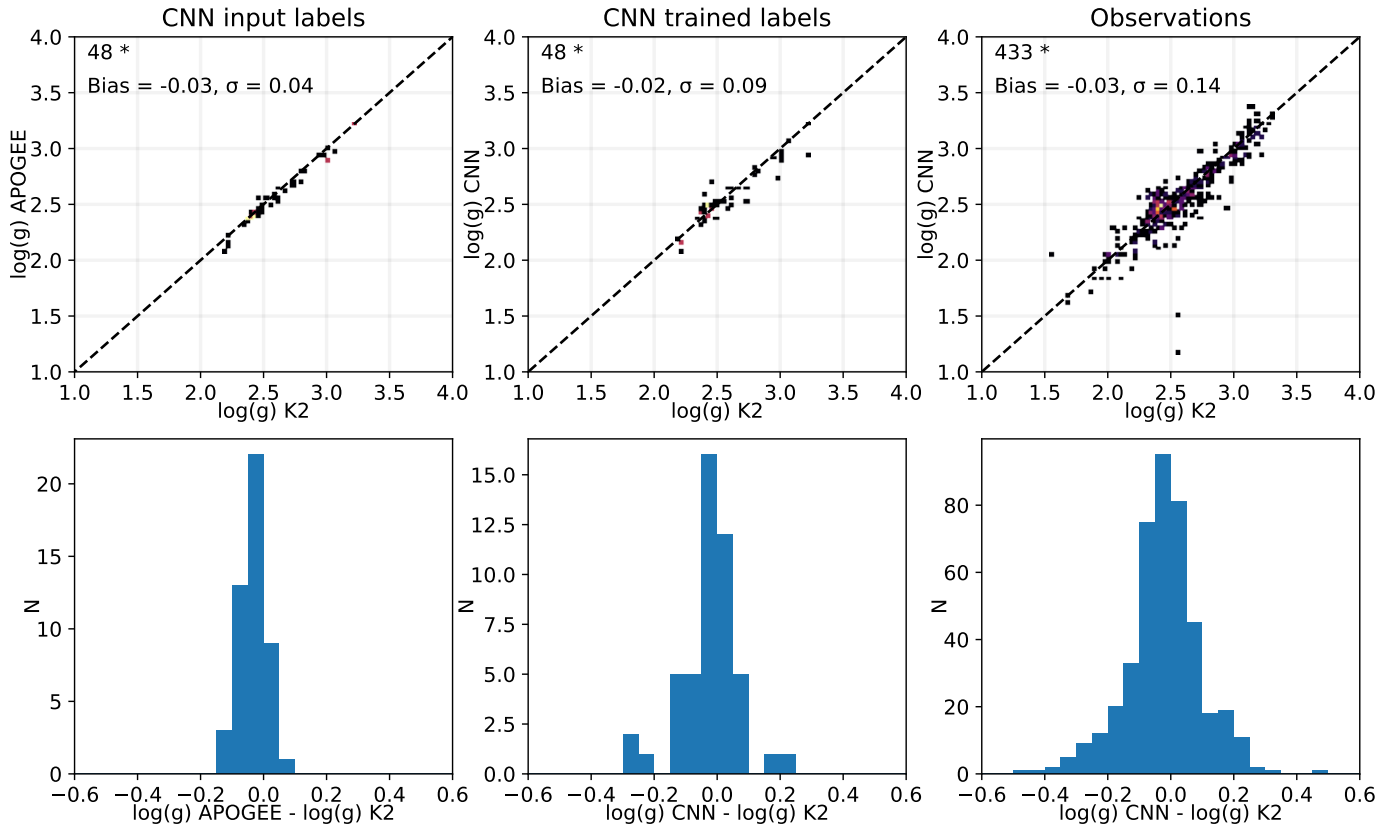


Fig. 14. Comparison of surface gravities from the present study with K2 asteroseismic data. Left panels: comparison with the $\log(g)$ labels from APOGEE DR16 used as input by our CNN. Middle panel: comparison with averaged labels trained by the CNN. Right panel: comparison with averaged $\log(g)$ predicted for common stars in the observed sample. Mean difference and scatter are indicated in the top left corner of each panel.

decrease when selecting stars with $S/N > 40$, but stays constant for $\log(g)$.

6.7. Comparison with RAVE DR6 $[\alpha/M]$ ratios

The RAVE spectra cover the near-infrared CaII triplet, which is a key spectral feature to put constraints on the overall α enrichment of stars. In this section, we compare the $[\alpha/M]$ derived in the present study by our CNN to the $[\alpha/Fe]$ derived in Steinmetz et al. (2020b) by a more classical approach (synthetic spectra grid + optimization method). Both quantities were derived using the same observed spectra.

In Fig. 21, we present an abundance pattern comparison between the present study ($[\alpha/M]$ vs. $[M/H]$) and RAVE DR6 ($[\alpha/Fe]$ vs. $[Fe/H]$), for 69 659 dwarfs and giants ($S/N > 20$). We adopt the same quality criteria presented in Steinmetz et al. (2020b) to select the best RAVE DR6 $[\alpha/Fe]$ ratios.

We first show a typical Kiel diagram for each sample (CNN top-left, RAVE DR6 top-right). Using our CNN approach with combined spectroscopy, photometry and astrometry, we are able to tackle the degeneracy caused by RAVE's narrow wavelength range, especially in the very cool regime.

The abundances derived by RAVE DR6 show a larger scatter at a given metallicity. In the metal-poor regime, the CNN results show a tight $[\alpha/M]$ sequence. Overall, both studies show the same main chemical features, for both gi-

ants and dwarfs. They also cover the same metallicity range. We note that in the metallicity range of $-1 < [M/H] < +0$ dex, the CNN $[M/H]$ present a shift of $+0.14$ dex with respect to RAVE DR6 $[Fe/H]$, while for both metal-poor and metal-rich tails, the bias is basically null. The differences in trends and zero-points originate from a different calibration between the two studies, one based on APOGEE data, while the RAVE DR6 is based on synthetic spectra grid.

6.8. Ability to detect exotic stars

Neural networks are particularly efficient in classifying objects. Also, peculiar stars are expected to be detected by such a machine-learning pipeline. By peculiar, we mean that the CNN is able to parameterize stars in regions where the training sample parameters space is poorly covered. We illustrate this point by the example of the known yellow supergiant (spectral type F3I, Houk 1978, Gaia_sourceid="5983723702088571392"), observed 6 times by the RAVE survey. The normalized RAVE DR6 spectra are presented in Fig. 22. The mean atmospheric parameters (and dispersion) derived by our CNN from the six repeats are the following: $T_{\text{eff}} = 5423 \pm 20$ K, $\log(g) = 1.02 \pm 0.02$, $[M/H] = -0.36 \pm 0.03$ dex. This star has been characterized as "normal" by RAVE DR6. Its Gaia DR2 parallax error is 10%. The average RAVE DR6 parameters derived with the BDASP pipeline (using Gaia DR2 and isochrone fitting) are the following: $T_{\text{eff}} = 5047$ K,

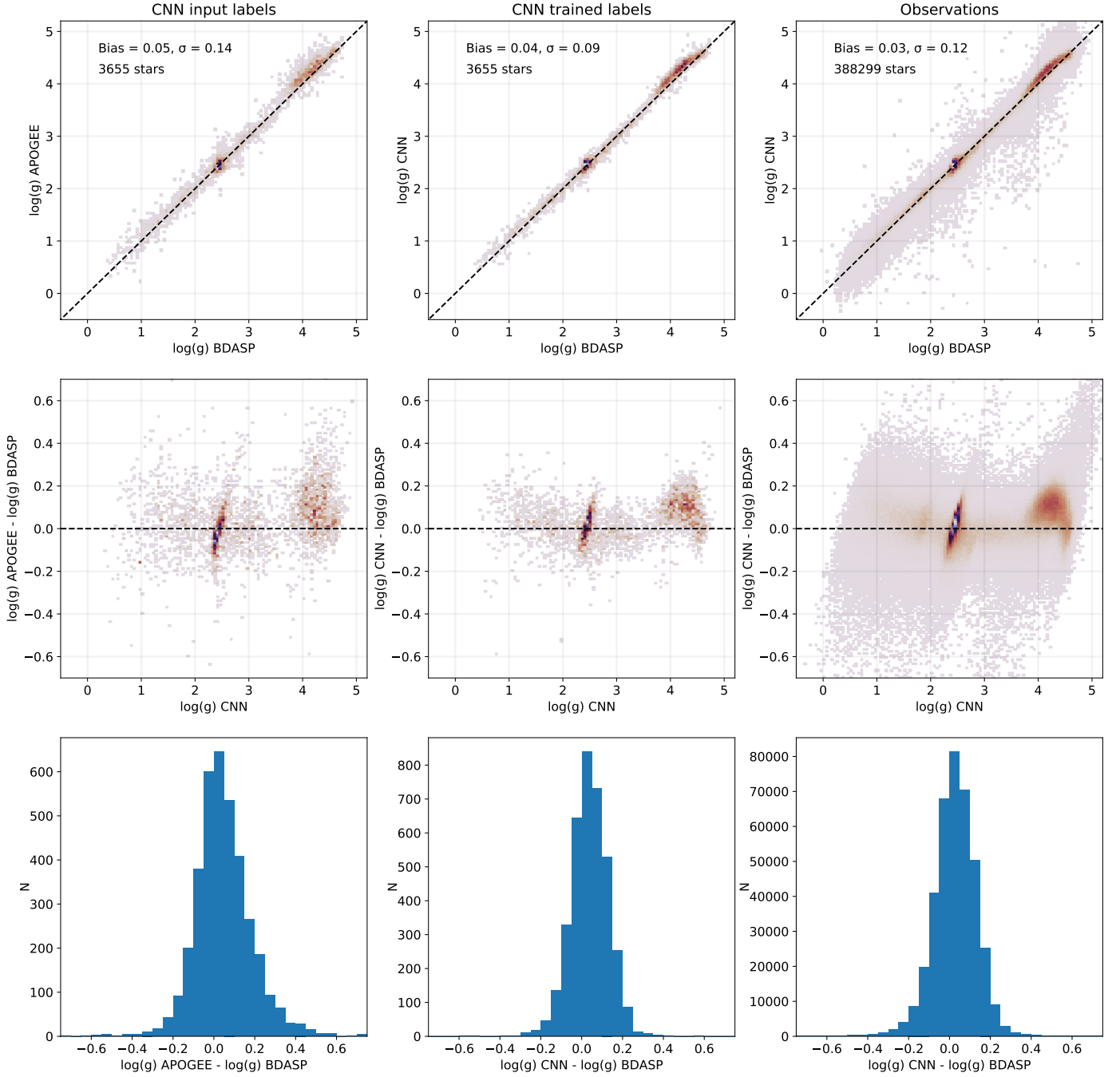


Fig. 15. Left column: Comparisons of the $\log(g)$ values used as input labels of our CNN (APOGEE DR16 $\log(g)$) with respect to $\log(g)$ values of Steinmetz et al. (2020b). We also show a residual plot and an histogram of the difference. Mean difference and scatter are indicated in the top-left corner. Middle column: we compare $\log(g)$ values trained by our CNN with respect to $\log(g)$ values of Steinmetz et al. (2020b). Right column: we compare the $\log(g)$ values derived by our CNN for 388 299 stars of our observed sample with respect to the $\log(g)$ values of Steinmetz et al. (2020b).

$\log(g) = 1.39$, $[M/H] = +0.28$ dex. In spite of the differences in approach, the CNN and BDASP methods tend to put this star in the same region of the Kiel diagram.

On the other hand, the RAVE DR6 parameters by the MADERA pipeline (pure spectroscopy) are the following: $T_{\text{eff}} = 5986$ K, $\log(g) = 3.63$, $[M/H] = +0.51$ dex. Those parameters are consistent to those derived by our CNN, only using spectroscopic data (no photometry or parallaxes): $T_{\text{eff}} = 6359$ K, $\log(g) = 3.82$, $[M/H] = +0.43$ dex.

7. Including photometry vs. not including photometry

We show here that adding absolute photometric magnitudes during the training phase of the CNN significantly improves the quality of the derived effective temperature and surface gravity, and to a lesser extent the overall metallicity. We recall that colors are key indicators of effective temperatures and, that colors and absolute magnitudes help to constrain surface gravities.

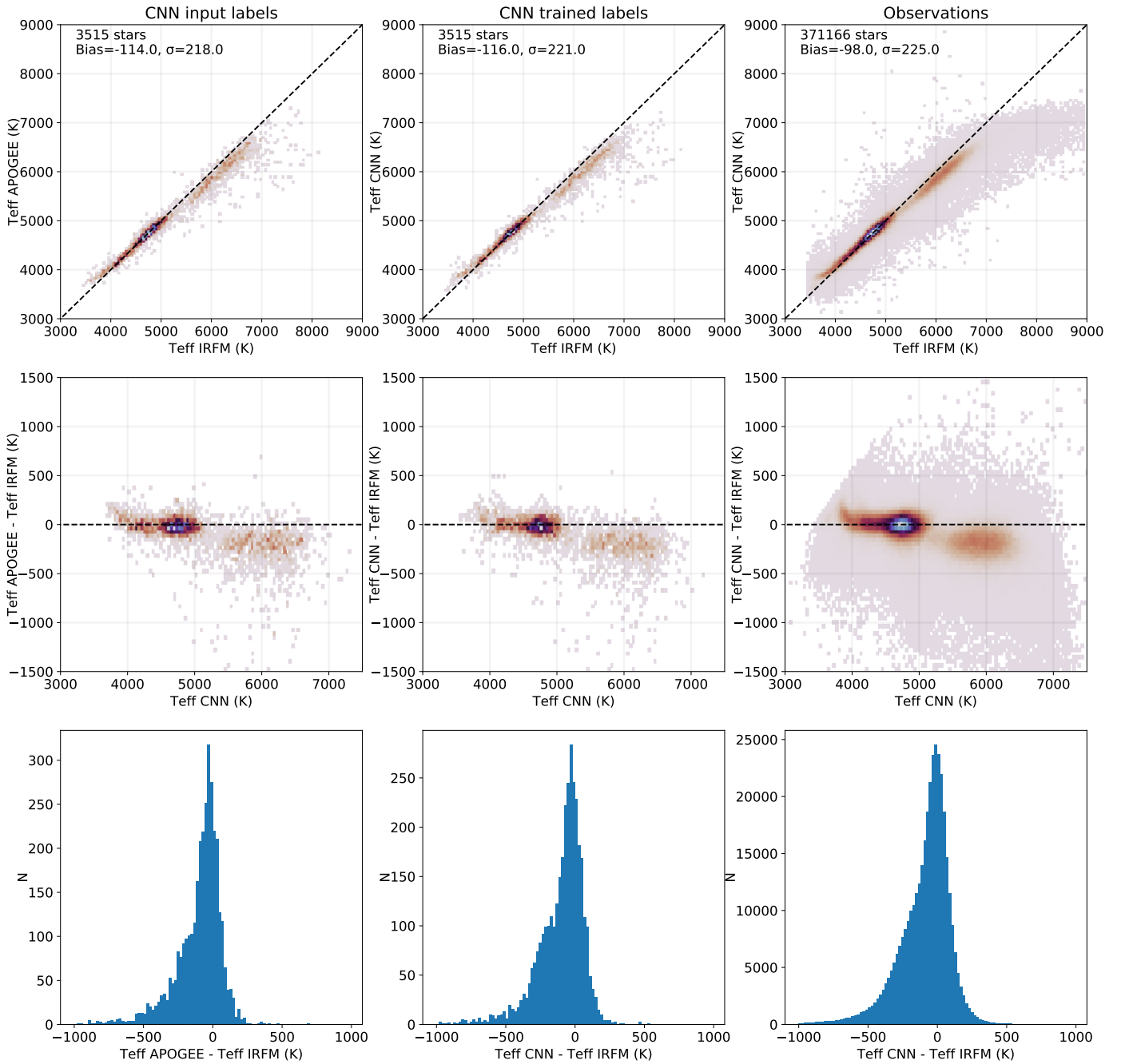


Fig. 16. Left column: comparisons of the input label T_{eff} for our CNN (APOGEE DR16 labels) with the IRFM temperatures of Steinmetz et al. (2020b). Mean difference and scatter are indicated in the top-left corner. We also show a residual plot and an histogram of the difference. Middle column: we compare the labels T_{eff} trained by the CNN with the IRFM temperatures of Steinmetz et al. (2020b). Right column: we compare the T_{eff} values derived for our whole observed data-set (for $S/N > 20$) with the IRFM temperatures of Steinmetz et al. (2020b).

To do so, we simply re-trained our CNN a hundred times, with the same overall architecture, but removing the photometric neurons, meaning that we only use pure spectroscopic data from RAVE. We kept the same training sample. We simultaneously predicted T_{eff} , $\log(g)$, $[M/H]$, $[Fe/H]$, plus individual abundances for the observed data.

In Fig. 23, we present the resulting Kiel diagram of T_{eff} and $\log(g)$, color-coded in $[M/H]$. We only show data with $S/N > 40$, i.e., stars with good observational data. Compared to the Kiel diagram derived including absolute magnitudes, the pure spectroscopic results still have all the

typical features, like the cool dwarf sequence, the turn-off, or the giant branch. On the other hand, the cool dwarfs sequence suffers from large scatter, while degeneracies appear for very cool giants (large $\log(g)$ scatter for a given T_{eff}). The red giant branch appears as a straight sequence. Finally, the metallicity sequence in the giant branch is not as well-defined as when absolute magnitudes are used. The wavelength range around the CaII triplet is known to suffer from degeneracies when deriving atmospheric parameters (Kordopatis et al. 2011a). We note that including absolute magnitudes helps us to break these degeneracies, without

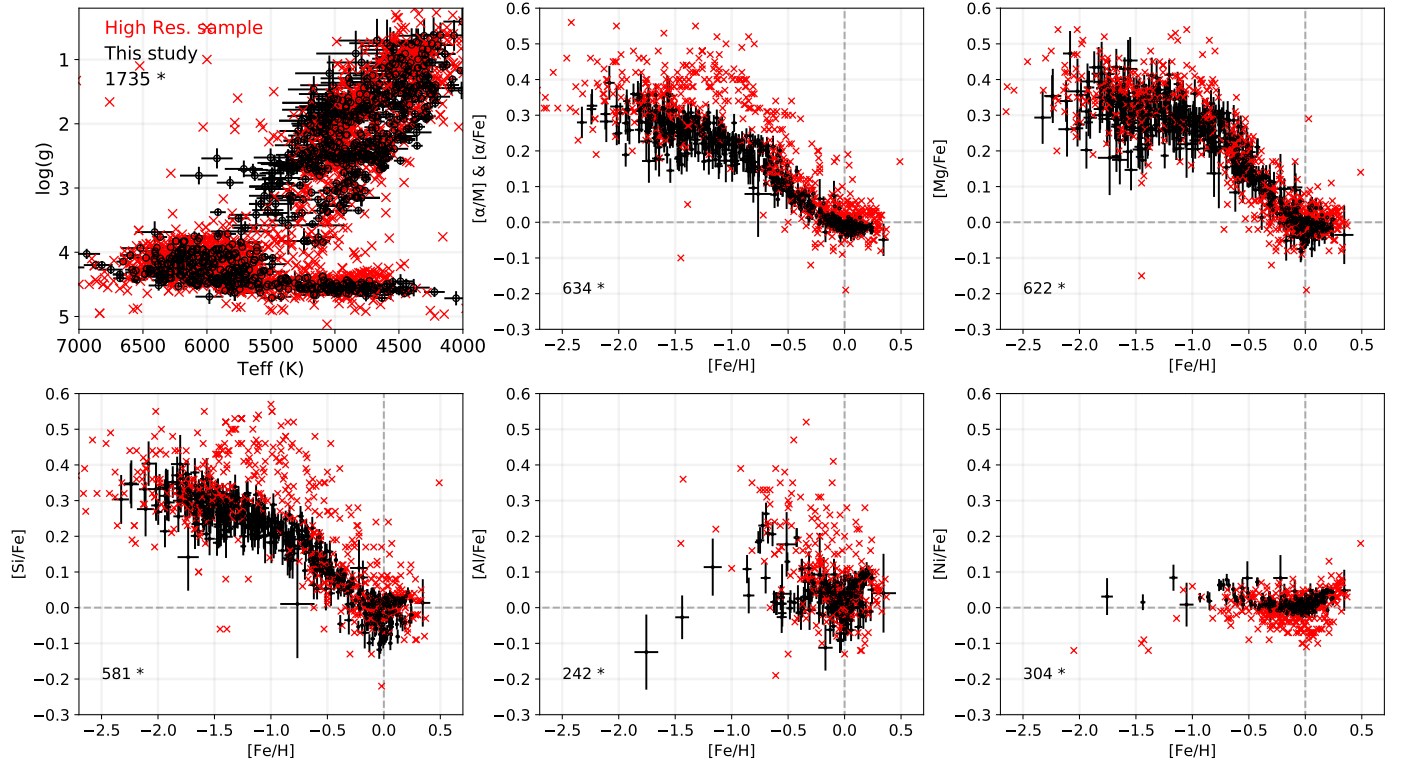


Fig. 17. Kiel diagram and chemical abundances patterns for stars in common between our study (black circles), and the literature (red crosses).

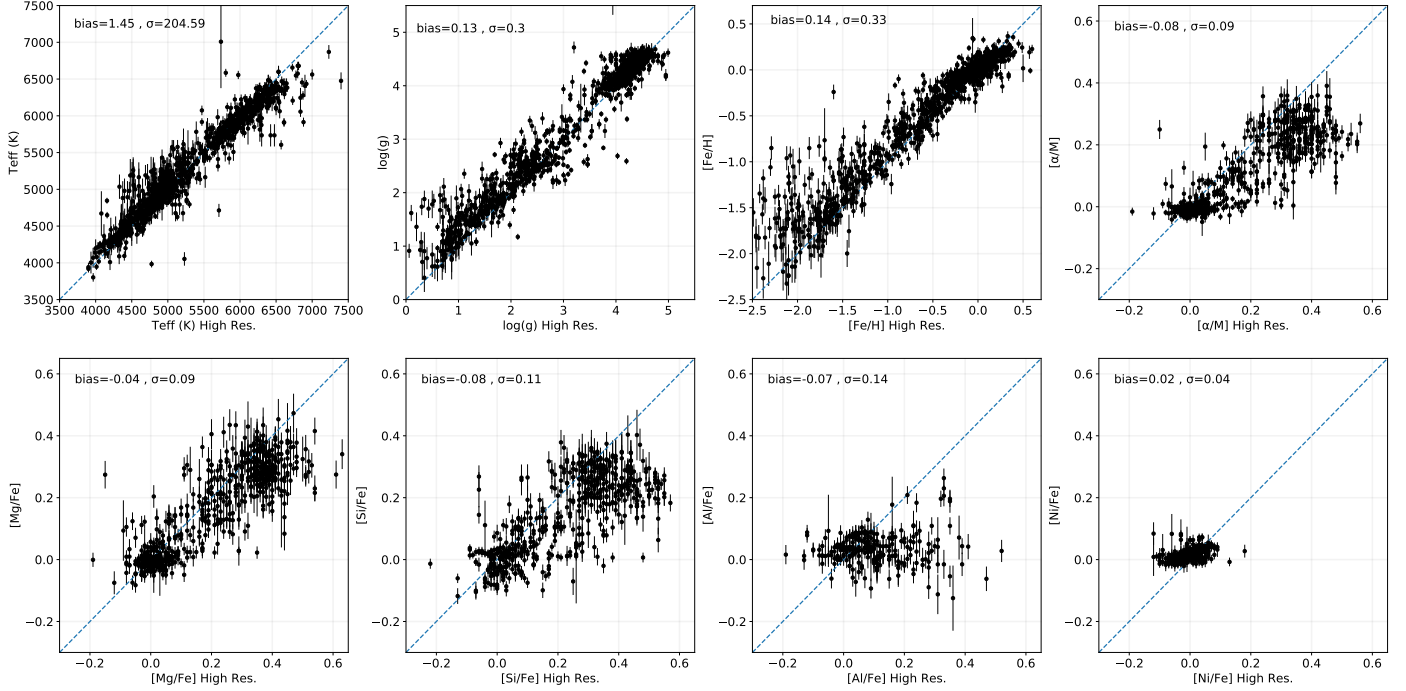


Fig. 18. Atmospheric parameters and chemical abundances derived by our CNN, as a function of values from the literature. Mean bias and dispersion are indicated in the top left corner of each panel.

applying any prior or restraining the parameter space of the training sample. The mean error in T_{eff} is increased by ~ 20 K when no absolute magnitudes are used.

We then compare our surface gravities with those from RAVE BDASP $\log(g)$. When using 2MASS+ALL_WISE+Gaia, one can see that the av-

erage difference between both studies is one quarter of the one based purely on spectroscopy, while the dispersion drops from 0.23 to 0.09 dex.

We then compare our purely spectroscopic $\log(g)$ values to those provided by K2. Without photometric input, the scatter is much larger (0.26 dex) with a tiny bias. We note

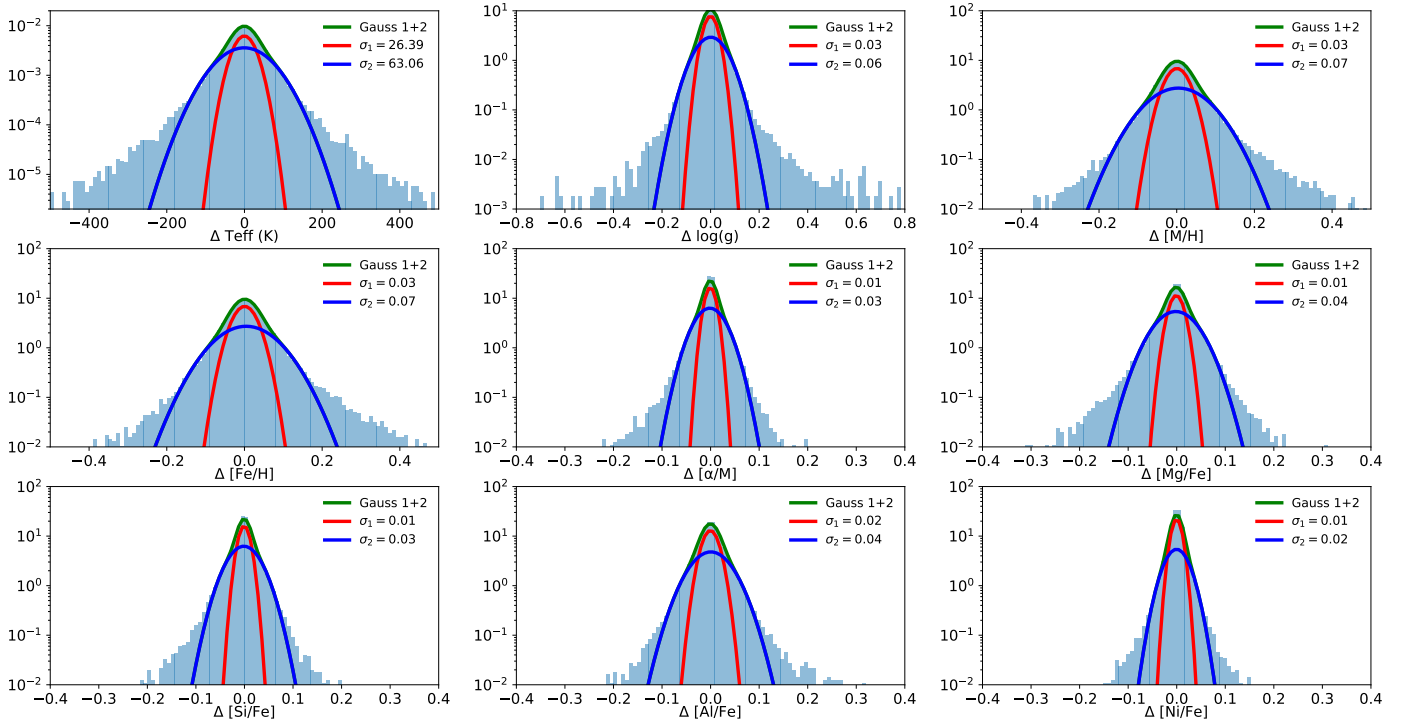


Fig. 19. Differences in atmospheric parameters and chemical abundances for 80 342 stars with several observations and $S/N > 20$.

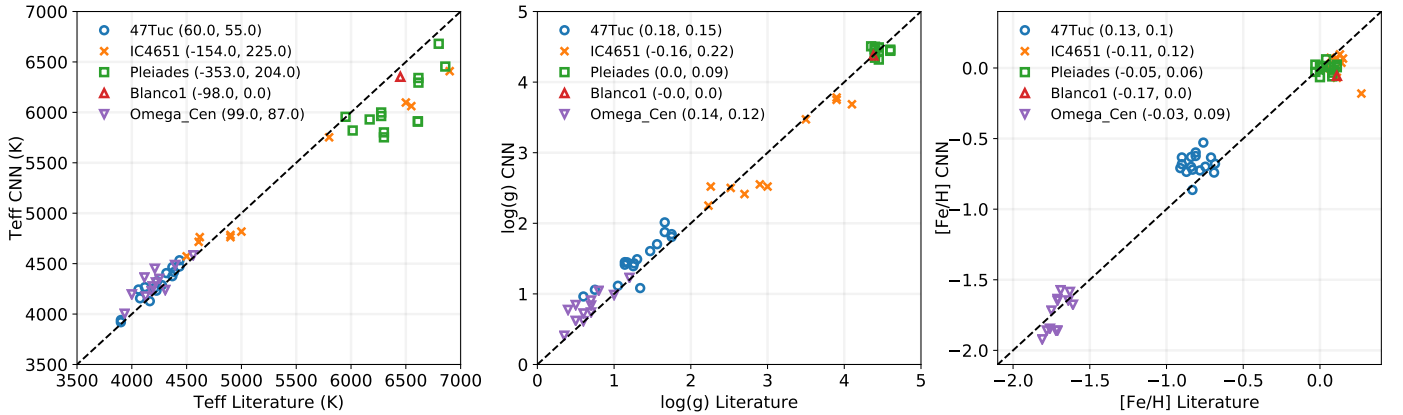


Fig. 20. Comparison of T_{eff} , $\log(g)$, and $[\text{Fe}/\text{H}]$ between the present study and compilation of five stellar clusters with common stars with RAVE: 47Tuc (\circ), IC4651 (\times), Pleiades (\square), Blanco1 (\triangle), and Omega Centauri (∇). The mean difference and dispersion are indicated together with the cluster name.

that the purely spectroscopic T_{eff} values show a slightly higher dispersion with respect to those derived including absolute magnitudes during the training phase.

We finally compare T_{eff} , $\log(g)$, and $[\text{M}/\text{H}]$ derived from purely spectroscopic data by our CNN to those of the high-resolution sample presented in Sect 6.4 (only stars with $S/N > 20$). Without absolute magnitudes, we observed a significantly larger dispersion in $\log(g)$ (0.58 dex) and bias (+0.26 dex), as compared to the high-resolution sample. This is also the case for the effective temperature, with a slightly larger bias (55 K instead of no bias) and a dispersion larger by 80 K. Finally, the metallicity derived purely by spectroscopic data suffers from a slightly higher bias and dispersion with respect to the literature sample. The main improvement is actually notable for $[\text{M}/\text{H}] < -1.5$ dex, consistent with previous remarks on the Kiel diagram.

With these comparisons we demonstrated that purely spectroscopic data can still provide quite satisfying outputs, but adding photometry and astrometric parallaxes provides a major gain with a strong increase in precision and accuracy, mainly for effective temperature and surface gravity. We are able to efficiently break the degeneracies in the $T_{\text{eff}} - \log(g)$ space, caused by limited spectral range of RAVE spectra, in particular in the cool regime.

8. Science verification

8.1. Abundance-kinematical properties of the Milky Way components

We investigate here some implications for the chemical and kinematical properties of the Milky Way. We adopted the kinematics from RAVE DR6 (Steinmetz et al. 2020b), and

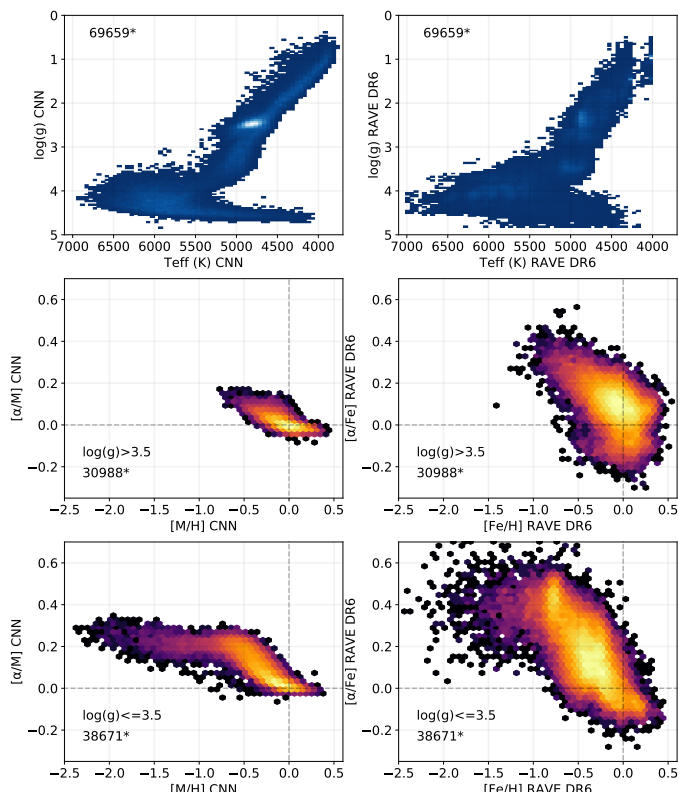


Fig. 21. Top panels: T_{eff} vs. $\log(g)$ for 69659 stars, derived with our CNN (left) and derived by RAVE DR6 (right). Middle panels: abundance pattern for 30988 dwarfs, derived by our CNN (left) and RAVE DR6 (right). Bottom panels: same plots for 38671 giants.

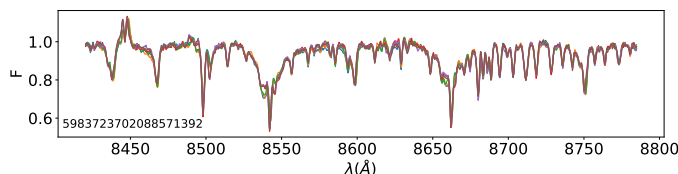


Fig. 22. Normalized RAVE DR6 spectra of the target Gaia "5983723702088571392". The six spectra are plotted in different colors.

followed the same approach as Gratton et al. (2003) and Boeche et al. (2013a). We first kinematically selected a thin disk component with low eccentricity stars ($e < 0.25$) and low maximum altitude ($Z_{\text{max}} < 0.8 \text{ kpc}$). We identified a dissipative collapse component, mainly composed of thick disk and halo stars with $e > 0.25$, $Z_{\text{max}} > 0.8 \text{ kpc}$, and $V_{\phi} > 40 \text{ km s}^{-1}$. Finally, we characterized an accretion component, composed of halo and accreted stars ($V_{\phi} < 40 \text{ km s}^{-1}$).

In Fig. 24, we present the $[\alpha/\text{M}]$ pattern for these three components for giant stars ($\log(g) < 3.5$). The thin disk is mainly confined to $[\text{M}/\text{H}] > -1 \text{ dex}$, while the dissipative collapse component shows a large metallicity range, a few metal-rich stars, including halo stars with metallicities higher than -2 dex , and a narrow $[\alpha/\text{M}]$ sequence. The accretion component is only composed of metal-poor stars, in the range $-2.0 < [\text{M}/\text{H}] < -0.5$. We note that the mean error on $[\text{M}/\text{H}]$ and $[\alpha/\text{M}]$ increases with decreasing metal-

licity for the three components. These findings are in good agreement with Boeche et al. (2013a).

We measured the gradients of V_{ϕ} vs. $[\text{M}/\text{H}]$ in both the thin disk and dissipative collapse components. The thin disk component shows an anti-correlation ($\nabla = -20 \text{ km s}^{-1}/\text{dex}$), while a strong correlation is visible in the dissipative collapse component ($\nabla = +54 \text{ km s}^{-1}/\text{dex}$). Such gradients are consistent with previous works, like for example Lee et al. (2011) with SEGUE data or Kordopatis et al. (2011b), despite different selection functions. Note, however, that the positive gradient in the dissipative collapse components results from the superposition of mono- $[\alpha/\text{M}]$ sub-populations with negative slopes, as recently shown using RAVE DR5 data (Wojno et al. 2018; Minchev et al. 2019). These simple science applications show the potential of the CNN abundances.

8.2. Chemical cartography of $[\alpha/\text{M}]$ ratio in the galactic discs

In this section, we investigate the spatial transition between the $[\alpha/\text{M}]$ -rich and $[\alpha/\text{M}]$ -poor populations of the Milky Way. We take again advantage of the orbital parameters provided by the 6th data release of RAVE (Steinmetz et al. 2020b). We present in Fig. 25 the behaviour of the $[\alpha/\text{M}]$ ratio as a function of $[\text{Fe}/\text{H}]$, for different bins of mean Galactocentric radii (R) and heights above the Galactic plane ($|Z|$). The figure shows hexagonal density maps and contour plots for a total of 185 569 giant stars with $S/N > 30$, parallax errors lower than 20%, and RAVE "n&o" classification. We observe that the $[\alpha/\text{M}]$ -poor population dominates at low Galactic heights ($|Z| < 0.5 \text{ kpc}$), while $[\alpha/\text{M}]$ -rich stars are mostly located at larger height above the plane ($|Z| > 0.5 \text{ kpc}$). In between, there is a very smooth transition. We note that such observations are also valid for the $[\text{Mg}/\text{Fe}]$ and $[\text{Si}/\text{Fe}]$ ratios, with slightly larger scatter. We find consistent results with the study of Hayden et al. (2015) based on APOGEE DR12. For the same Galactic volume, our results are a good match with the recent study by Queiroz et al. (2019) based on APOGEE DR16.

We show that we are able to complement RAVE DR6, providing chemical abundance trends for a larger sample of stars, with improved precision.

9. Caveats

The present project relies entirely on the cross-match between a few thousand RAVE and APOGEE targets, which, together with the limitations of the two respective surveys, results in a number of possible caveats:

- The spectral range of RAVE spectra, $[8410 - 8795] \text{ \AA}$, contains plenty of features to derive $[\alpha/\text{M}]$ ratios, such as Ca, Ti, Mg, Si, and O spectral lines. The $[\alpha/\text{M}]$ labels adopted here come from the DR16 of APOGEE. This survey uses a different wavelength range ($1.51 - 1.70 \mu\text{m}$), but still, its wavelength coverage contains similar elements as RAVE contributing to the $[\alpha/\text{M}]$ mixture, except Ne and S. On the other hand, it is known that the most significant contributors of the spectral features are Ca, Ti, Si, O, and Mg. In this context, using the RAVE spectral range to constrain $[\alpha/\text{M}]$ is reasonable.
- We clearly have a lack of stars at low metallicity ($[\text{M}/\text{H}] \lesssim -1$) in the training sample, coming mainly from the fact that we have few metal-poor stars in

RAVE (Matijević et al. 2017) and in the cross-match with APOGEE DR16. The mapping of the parameters space for those stars is quite limited. For future studies, one should carefully build a training sample with good mapping of the parameters in the metal-poor regime. More and more metal-poor stars are being observed, for example in the Pristine Survey (Starkenburg et al. 2017; Youakim et al. 2017), and they are key stars for a more homogeneous mapping of the parameters space.

- Out of the approximately 400 000 stars of the APOGEE survey DR16, our training sample contains roughly 4 000 stars in common with the RAVE survey. It is clear that the APOGEE and RAVE surveys are characterized by different selection functions. This will lead to astrophysical biases in the selection function of the training. This is a caveat in our study, but the goal is for the moment not to characterize such biases, and will be the object of a future study. For the future, the community will have to put particular efforts in creating unbiased training samples, especially for the next generation of spectroscopic surveys, like 4MOST.

10. Database and public code

We present here our catalog of atmospheric parameters (T_{eff} , $\log(g)$, $[\text{M}/\text{H}]$), and chemical abundances ($[\text{Fe}/\text{H}]$, $[\alpha/\text{M}]$, $[\text{Si}/\text{Fe}]$, $[\text{Mg}/\text{Fe}]$, $[\text{Al}/\text{Fe}]$, $[\text{Ni}/\text{Fe}]$), for 420 165 stars, summarized in Table 1. The data table is available on: doi://10.17876/rave/dr.6/19.

The CNN architecture and weights will be publicly available.

11. Conclusion

We list here our main results:

- Based of APOGEE DR16, we built a training sample composed of 3 904 stars in common with RAVE DR6. These stars have high quality atmospheric parameters and chemical abundances for $[\text{Fe}/\text{H}]$, $[\alpha/\text{M}]$, $[\text{Si}/\text{Fe}]$, $[\text{Mg}/\text{Fe}]$, $[\text{Al}/\text{Fe}]$, and $[\text{Ni}/\text{Fe}]$, which we use as labels.
- We built a CNN using the Keras libraries in Python to train the labels defined above.
- Using these trained labels, we predicted atmospheric parameters and chemical abundances for 420 165 RAVE spectra. The results are available online. Our catalog covers a larger range of S/N than RAVE DR6, and extends the scientific output of the RAVE spectra.
- We used ALL_WISE W1&2, 2MASS JHK_s , and Gaia DR2 G , G_{BP} , and G_{RP} apparent magnitudes, and extinction estimates to derive absolute magnitudes. We included them in the training process and showed that CNNs are efficient in combining spectroscopic and photometric data. We drastically gain in precision and accuracy, especially in T_{eff} and $\log(g)$, when spectral features are too degenerate (cool main sequence stars, metal-poor giants, and very cool giants). We demonstrated that such a comprehensive combination of spectra, photometry, and parallaxes allows us to efficiently break degeneracies when the spectral range is too narrow to provide strong constraints on surface gravity.
- Performing a hundred training phases, we derived errors of the atmospheric parameters, which typically amount to 60 K in T_{eff} , 0.06 in $\log(g)$, and 0.02-0.04 dex for

individual chemical abundances. Such high precision is realistic because the network is able to learn on the low- and high- α sequences in the Milky Way disk.

- We show that for stars with several observations, the network is able to provide precise atmospheric parameters and abundances among the repeats, typically precise to 50 K in T_{eff} and 0.03-0.05 dex in abundances.
- We have shown that the surface gravities match nicely with more than 430 asteroseismic gravities from the K2 space mission within 0.14 dex dispersion and no bias.
- We compared our effective temperature and surface gravities with respect to both the IRFM T_{eff} and $\log(g)$ from the DR6 of RAVE, and were able to characterise the systematics between the two studies.
- It is important to note that different trends and zero-point offsets between this work and external studies primarily reflect different calibrations of these surveys. A systematic comparison between different surveys is therefore crucial.
- The CNN architecture and weights will be publicly available.
- Despite quite low number statistics in the training sample with respect to the number of free parameters to fit, we showed that such an approach can provide solid scientific output.

Our study shows that CNNs are particularly efficient in transferring knowledge from one survey at high resolution like APOGEE to another at lower resolution, like RAVE. This study gives good insights for on-going and future spectroscopic surveys, like Gaia-RVS and 4MOST. Gaia-RVS spectra are expected to be very similar to those of RAVE ($R \sim 11400$) and we showed that adding photometry breaks spectral degeneracies, and photometry will be available for all RVS targets. Efficient training of Gaia-RVS data based on higher-resolution surveys could deliver atmospheric parameters and abundances for a larger number of RVS stars, as it is the case for RAVE in the present paper. The low-resolution 4MOST spectra will cover a much larger spectral range (4000 – 9000 Å) at a slightly lower resolution than Gaia for the 4MIDABLE-LR low-resolution survey (Chiappini et al. 2019), and Gaia photometry will also be available for all targets. Additional constraints could then be put on the derivation of T_{eff} and $\log(g)$ by coupling spectroscopy, photometry, and astrometry. Such surveys will deliver millions of spectra that can be analysed in only a few minutes on a single Graphics Processing Unit, once the labels are trained.

Acknowledgements. Funding for RAVE has been provided by: the Leibniz-Institut für Astrophysik Potsdam (AIP); the Australian Astronomical Observatory; the Australian National University; the Australian Research Council; the French National Research Agency (Programme National Cosmologie et Galaxies (PNCG) of CNRS/INSU with INP and IN2P3, co-funded by CEA and CNES); the German Research Foundation (SPP 1177 and SFB 881); the European Research Council (ERC-StG 240271 Galactica); the Istituto Nazionale di Astrofisica at Padova; The Johns Hopkins University; the National Science Foundation of the USA (AST-0908326); the W. M. Keck foundation; the Macquarie University; the Netherlands Research School for Astronomy; the Natural Sciences and Engineering Research Council of Canada; the Slovenian Research Agency (research core funding no. P1-0188); the Swiss National Science Foundation; the Science & Technology Facilities Council of the UK; Opticon; Strasbourg Observatory; and the Universities of Basel, Groningen, Heidelberg, and Sydney. TZ acknowledges financial support of the Slovenian Research Agency (research core funding No.

Col	Format	Units	Label	Explanations
1	char	-	rave_obs_id	RAVE Obs ID
2	char	-	sourceid	Gaia Source ID
3	float	K	teff	Effective temperature
4	float	K	eteff	Error of T_{eff}
5	int	-	flag_teff	Boundary flag for T_{eff}
6	float	cm s ⁻²	logg	Surface gravity
7	float	cm s ⁻²	elogg	Error on $\log(g)$
8	int	-	flag_logg	Boundary flag for $\log(g)$
9	float	dex	mh	Overall metallicity
10	float	dex	emh	Error on [M/H]
11	int	-	flag_mh	Boundary flag for [M/H]
12	float	dex	feh	[Fe/H] ratio
13	float	dex	efeh	Error on [Fe/H]
14	int	-	flag_feh	Boundary flag for [Fe/H]
15	float	dex	alpham	[α /M] ratio
16	float	dex	ealpham	Error on [α /M]
17	int	-	flag_alpham	Boundary flag for [α /M]
18	float	dex	sife	[Si/Fe] ratio
19	float	dex	esife	Error on [Si/Fe]
20	int	-	flag_sife	Boundary flag for [Si/Fe]
21	float	dex	mgfe	[Mg/Fe] ratio
22	float	dex	emgfe	Error on [Mg/Fe]
23	int	-	flag_mgfe	Boundary flag for [Mg/Fe]
24	float	dex	alfe	[Al/Fe] ratio
25	float	dex	ealfe	Error on [Al/Fe]
26	int	-	flag_alfe	Boundary flag for [Al/Fe]
27	float	dex	nife	[Ni/Fe] ratio
28	float	dex	enife	Error on [Ni/Fe]
29	int	-	flag_nife	Boundary flag for [Ni/Fe]
30	float	/pix	snr	Signal-to-noise ratio

Table 1. Atmospheric parameters, chemical abundances and boundary flags of the publicly available online catalog for 420 165 stars.

P1-0188) and of the ESA project PHOT2CHEM (C4000127986). This work has made use of data from the European Space Agency (ESA) mission Gaia (<http://www.cosmos.esa.int/gaia>), processed by the Gaia Data Processing and Analysis Consortium (DPAC, <http://www.cosmos.esa.int/web/gaia/dpac/consortium>). Funding for the DPAC has been provided by national institutions, in particular the institutions participating in the Gaia Multilateral Agreement. This publication makes use of data products from the Wide-field Infrared Survey Explorer, which is a joint project of the University of California, Los Angeles, and the Jet Propulsion Laboratory/California Institute of Technology, funded by the National Aeronautics and Space Administration. This publication makes use of data products from the Two Micron All Sky Survey, which is a joint project of the University of Massachusetts and the Infrared Processing and Analysis Center/California Institute of Technology, funded by the National Aeronautics and Space Administration and the National Science Foundation.

References

- Adibekyan, V. Z., Sousa, S. G., Santos, N. C., et al. 2012, *A&A*, 545, A32
- Ahumada, R., Allende Prieto, C., Almeida, A., et al. 2019, arXiv e-prints, arXiv:1912.02905
- Allende Prieto, C., Beers, T. C., Wilhelm, R., et al. 2006, *ApJ*, 636, 804
- Anders, F., Khalatyan, A., Chiappini, C., et al. 2019, *A&A*, 628, A94
- Antoja, T., Kordopatis, G., Helmi, A., et al. 2017, *A&A*, 601, A59
- Arenou, F., Luri, X., Babusiaux, C., et al. 2018, *A&A*, 616, A17
- Bensby, T., Bergemann, M., Rybizki, J., et al. 2019, *The Messenger*, 175, 35
- Bensby, T., Feltzing, S., & Oey, M. S. 2014, *A&A*, 562, A71
- Bialek, S., Fabbro, S., Venn, K. A., et al. 2019, arXiv e-prints, arXiv:1911.02602
- Bijaoui, A., Recio-Blanco, A., De Laverny, P., & Ordenovic, C. 2012, *Statistical Methodology*, 9, 55
- Boeche, C., Chiappini, C., Minchev, I., et al. 2013a, *A&A*, 553, A19
- Boeche, C. & Grebel, E. K. 2018, *SP_Ace: Stellar Parameters And Chemical abundances Estimator*
- Boeche, C., Siebert, A., Piffl, T., et al. 2014, *A&A*, 568, A71
- Boeche, C., Siebert, A., Piffl, T., et al. 2013b, *A&A*, 559, A59
- Boeche, C., Siebert, A., Williams, M., et al. 2011, *AJ*, 142, 193
- Buder, S., Asplund, M., Duong, L., et al. 2018, *MNRAS*, 478, 4513
- Buder, S., Lind, K., Ness, M. K., et al. 2019, *A&A*, 624, A19
- Carretta, E., Bragaglia, A., Gratton, R., & Lucatello, S. 2009, *A&A*, 505, 139
- Casagrande, L., Portinari, L., & Flynn, C. 2006, *MNRAS*, 373, 13
- Casagrande, L., Ramírez, I., Meléndez, J., Bessell, M., & Asplund, M. 2010, *A&A*, 512, A54
- Casey, A. R., Hawkins, K., Hogg, D. W., et al. 2017, *ApJ*, 840, 59
- Casey, A. R., Hogg, D. W., Ness, M., et al. 2016, arXiv e-prints, arXiv:1603.03040
- Chiappini, C., Minchev, I., Starkenburg, E., et al. 2019, *The Messenger*, 175, 30
- Chollet, F. et al. 2015, *Keras*, <https://github.com/fchollet/keras>
- Cireşan, D. C., Meier, U., Masci, J., Gambardella, L. M., & Schmidhuber, J. 2011, arXiv e-prints, arXiv:1102.0183
- Dalton, G., Trager, S., Abrams, D. C., et al. 2018, in *Society of Photo-Optical Instrumentation Engineers (SPIE) Conference Series*, Vol. 10702, *Proc. SPIE*, 107021B
- de Jong, R. S., Agertz, O., Berbel, A. A., et al. 2019, *The Messenger*, 175, 3
- Fabbro, S., Venn, K. A., O’Brien, T., et al. 2018, *MNRAS*, 475, 2978
- Ford, A., Jeffries, R. D., & Smalley, B. 2005, *MNRAS*, 364, 272
- Freeman, K. & Bland-Hawthorn, J. 2002, *ARA&A*, 40, 487
- Funayama, H., Itoh, Y., Oasa, Y., et al. 2009, *PASJ*, 61, 931

- Gaia Collaboration, Babusiaux, C., van Leeuwen, F., et al. 2018a, *A&A*, 616, A10
- Gaia Collaboration, Brown, A. G. A., Vallenari, A., et al. 2018b, *A&A*, 616, A1
- García Pérez, A. E., Allende Prieto, C., Holtzman, J. A., et al. 2016, *AJ*, 151, 144
- Gilmore, G., Randich, S., Asplund, M., et al. 2012, *The Messenger*, 147, 25
- Gratton, R. G., Carretta, E., Desidera, S., et al. 2003, *A&A*, 406, 131
- Guiglion, G., de Laverny, P., Recio-Blanco, A., et al. 2016, *A&A*, 595, A18
- Hanke, M., Hansen, C. J., Koch, A., & Grebel, E. K. 2018, *A&A*, 619, A134
- Hayden, M. R., Bovy, J., Holtzman, J. A., et al. 2015, *ApJ*, 808, 132
- Houk, N. 1978, Michigan catalogue of two-dimensional spectral types for the HD stars
- Johnson, C. I. & Pilachowski, C. A. 2010, *ApJ*, 722, 1373
- Kordopatis, G., Binney, J., Gilmore, G., et al. 2015, *MNRAS*, 447, 3526
- Kordopatis, G., Gilmore, G., Steinmetz, M., et al. 2013, *AJ*, 146, 134
- Kordopatis, G., Recio-Blanco, A., de Laverny, P., et al. 2011a, *A&A*, 535, A106
- Kordopatis, G., Recio-Blanco, A., de Laverny, P., et al. 2011b, *A&A*, 535, A107
- Kos, J., Lin, J., Zwitter, T., et al. 2017, *MNRAS*, 464, 1259
- Kunder, A., Kordopatis, G., Steinmetz, M., et al. 2017, *AJ*, 153, 75
- Lee, Y. S., Beers, T. C., An, D., et al. 2011, *ApJ*, 738, 187
- Leung, H. W. & Bovy, J. 2019, *MNRAS*, 483, 3255
- Lindgren, L., Hernández, J., Bombrun, A., et al. 2018, *A&A*, 616, A2
- Matijević, G., Chiappini, C., Grebel, E. K., et al. 2017, *A&A*, 603, A19
- Matteucci, F. & Francois, P. 1989, *MNRAS*, 239, 885
- McMillan, P. J., Kordopatis, G., Kunder, A., et al. 2018, *MNRAS*, 477, 5279
- Minchev, I., Chiappini, C., Martig, M., et al. 2014, *ApJ*, 781, L20
- Minchev, I., Matijević, G., Hogg, D. W., et al. 2019, *MNRAS*, 487, 3946
- Morel, T. & Miglio, A. 2012, *MNRAS*, 419, L34
- Ness, M., Hogg, D. W., Rix, H. W., Ho, A. Y. Q., & Zasowski, G. 2015, *ApJ*, 808, 16
- Nordström, B., Mayor, M., Andersen, J., et al. 2004, *A&A*, 418, 989
- Pancino, E. & Gaia-ESO Survey consortium, o. b. o. t. 2012, *ArXiv e-prints*
- Pasquini, L., Randich, S., Zoccali, M., et al. 2004, *A&A*, 424, 951
- Pinsonneault, M. H., Elsworth, Y. P., Tayar, J., et al. 2018, *The Astrophysical Journal Supplement Series*, 239, 32
- Queiroz, A. B. A., Anders, F., Chiappini, C., et al. 2019, *arXiv e-prints*, arXiv:1912.09778
- Queiroz, A. B. A., Anders, F., Santiago, B. X., et al. 2018, *MNRAS*, 476, 2556
- Recio-Blanco, A., Bijaoui, A., & de Laverny, P. 2006, *MNRAS*, 370, 141
- Reddy, B. E., Lambert, D. L., & Prieto, C. A. 2006, *VizieR Online Data Catalog*, J/MNRAS/367/1329
- Reddy, B. E., Tomkin, J., Lambert, D. L., & Allende Prieto, C. 2003, *VizieR Online Data Catalog*, J/MNRAS/340/304
- Ruchti, G. R., Fulbright, J. P., Wyse, R. F. G., et al. 2010, *ApJ*, 721, L92
- Ruchti, G. R., Fulbright, J. P., Wyse, R. F. G., et al. 2011, *ApJ*, 743, 107
- Santiago, B. X., Brauer, D. E., Anders, F., et al. 2016, *A&A*, 585, A42
- Skrutskie, M. F., Cutri, R. M., Stiening, R., et al. 2006, *AJ*, 131, 1163
- Smiljanic, R., Romano, D., Bragaglia, A., et al. 2016, *A&A*, 589, A115
- Soubiran, C. & Girard, P. 2005, *A&A*, 438, 139
- Starkenburg, E., Martin, N., Youakim, K., et al. 2017, *MNRAS*, 471, 2587
- Steinmetz, M. 2003, in *Astronomical Society of the Pacific Conference Series*, Vol. 298, *GAIA Spectroscopy: Science and Technology*, ed. U. Munari, 381
- Steinmetz, M., Guiglion, G., McMillan, P. J., et al. 2020a, *arXiv e-prints*, arXiv:2002.04512
- Steinmetz, M., Matijević, G., Enke, H., et al. 2020b, *arXiv e-prints*, arXiv:2002.04377
- Steinmetz, M., Zwitter, T., Siebert, A., et al. 2006, *AJ*, 132, 1645
- Ting, Y.-S., Conroy, C., Rix, H.-W., & Cargile, P. 2019, *ApJ*, 879, 69
- Valenti, J. A. & Fischer, D. A. 2005, *ApJS*, 159, 141
- Valenti, J. A. & Piskunov, N. 1996, *A&AS*, 118, 595
- Valentini, M., Chiappini, C., Davies, G. R., et al. 2017, *A&A*, 600, A66
- Van Cleve, J. E., Howell, S. B., Smith, J. C., et al. 2016, *PASP*, 128, 075002
- Wang, L., Wang, W., Wu, Y., et al. 2016, *AJ*, 152, 6
- Wojno, J., Kordopatis, G., Steinmetz, M., et al. 2018, *MNRAS*, 477, 5612
- Wright, E. L., Eisenhardt, P. R. M., Mainzer, A. K., et al. 2010, *AJ*, 140, 1868
- Wyse, R. F. G. & Gilmore, G. 1988, *AJ*, 95, 1404
- Yanny, B., Rockosi, C., Newberg, H. J., et al. 2009, *AJ*, 137, 4377
- Yoshii, Y. 1981, *A&A*, 97, 280
- Youakim, K., Starkenburg, E., Aguado, D. S., et al. 2017, *MNRAS*, 472, 2963
- Zhang, X., Zhao, G., Yang, C. Q., Wang, Q. X., & Zuo, W. B. 2019, *PASP*, 131, 094202
- Zwitter, T., Siebert, A., Munari, U., et al. 2008, *AJ*, 136, 421

- ¹ Leibniz-Institut für Astrophysik Potsdam (AIP), An der Sternwarte 16, 14482 Potsdam, Germany
e-mail: gguiglion@aip.de
- ² Astronomisches Rechen-Institut, Zentrum für Astronomie der Universität Heidelberg, Mönchhofstr. 12–14, 69120 Heidelberg, Germany
- ³ Lund Observatory, Department of Astronomy and Theoretical Physics, Lund University, Box 43, 22100 Lund, Sweden
- ⁴ Université Côte d’Azur, Observatoire de la Côte d’Azur, CNRS, Laboratoire Lagrange, France
- ⁵ Saint Martin’s University, 5000 Abbey Way SE, Lacey, WA, 98503, USA
- ⁶ University of Ljubljana, Faculty of Mathematics and Physics, Jadranska 19, SI-1000 Ljubljana, Slovenia
- ⁷ Institut de Ciències del Cosmos, Universitat de Barcelona (IEEC-UB), Martí i Franquès 1, 08028 Barcelona, Spain
- ⁸ Observatoire astronomique de Strasbourg, Université de Strasbourg, CNRS, 11 rue de l’Université, F-67000 Strasbourg, France
- ⁹ The Johns Hopkins University, Department of Physics and Astronomy, 3400 N. Charles Street, Baltimore, MD 21218, USA
- ¹⁰ Kavli Institute for Theoretical Physics, University of California, Santa Barbara, CA 93106, USA
- ¹¹ Sydney Institute for Astronomy, School of Physics, The University of Sydney, NSW 2006, Australia
- ¹² E.A. Milne Centre for Astrophysics, University of Hull, Hull, HU6 7RX, United Kingdom
- ¹³ Department of Physics and Astronomy, University of Victoria, Victoria, BC, Canada V8P5C2
- ¹⁴ CYM Physics Building, The University of Hong Kong, Pokfulam, Hong Kong SAR, PRC
- ¹⁵ The Laboratory for Space Research, Hong Kong University, Cyberport 4, Hong Kong SAR, PRC
- ¹⁶ Department of Physics and Astronomy, Macquarie University, Sydney, NSW 2109, Australia
- ¹⁷ Western Sydney University, Locked bag 1797, Penrith South, NSW 2751, Australia
- ¹⁸ Mullard Space Science Laboratory, University College London, Holmbury St Mary, Dorking, RH5 6NT, UK

Appendix A: Chemical abundance patterns of [Mg/Fe], [Si/Fe], [Al/Fe] and [Ni/Fe]

In this section, we present chemical abundance patterns of [Mg/Fe], [Si/Fe], [Al/Fe], and [Ni/Fe] as a function of [Fe/H] in the training and observed samples ($S/N > 30$ and “n” stars). Fig. A.1 and Fig. A.2 present [Mg/Fe] and [Si/Fe] abundances patterns for 301 076 stars. The trends of both elements look pretty similar to the trends of $[\alpha/M]$ presented in Fig. 11, Si and Mg being α -elements. In Fig. A.3, we present the chemical abundance patterns of [Al/Fe] of the same 301 076 stars. For $[Fe/H] > -1$ dex,

[Al/Fe] behaves like an α -element (consistent with previous findings in the literature, see for example Smiljanic et al. 2016). For $[\text{Fe}/\text{H}] < -1$, one can see that the [Al/Fe] ratio drops to solar and even negative ratios. It is mainly driven by the very few stars we have in the training sample, exhibiting low-[Al/Fe] ratios. One should be particularly careful when using such [Al/Fe] abundances. In Fig. A.4, we present [Ni/Fe] ratios for 301 076 stars. This ratio is rather flat with $[\text{Fe}/\text{H}]$, as expected for such an Fe-peak element.

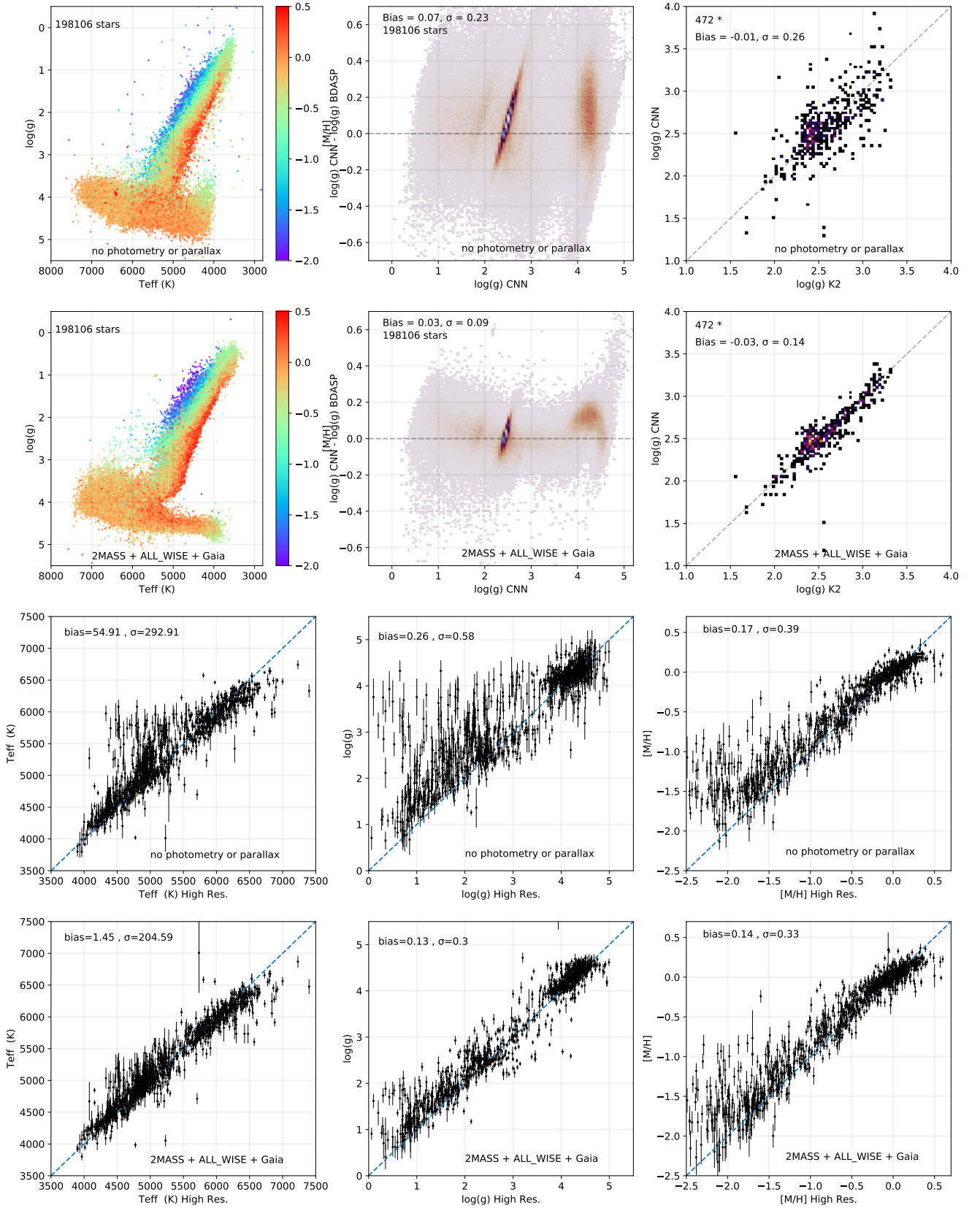


Fig. 23. Systematic comparisons of parameters from our CNN with or without photometry (2MASS+ALL_WISE+GaiaDR2) and astrometry (Gaia DR2). Top left panels: The Kiel diagrams are color-coded in $[M/H]$ for 198 106 stars ("n&o" classification) with $S/N > 40$ and parallax errors lower than 20%; Top middle panels: Comparison of $\log(g)$ with respect to RAVE DR6 $\log(g)$ for the same stars; Top right panels: Comparison of CNN $\log(g)$ values with respect to K2 $\log(g)$ values; Bottom panels: Comparisons of CNN T_{eff} , $\log(g)$, and $[M/H]$ values with respect to the high-resolution sample (one-to-one relations).

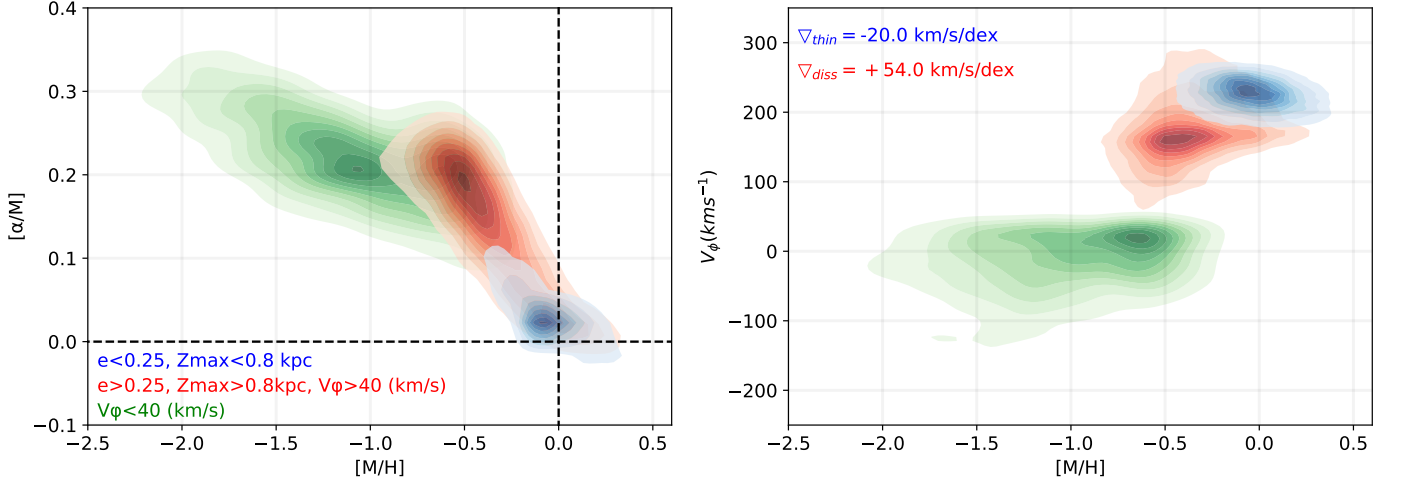


Fig. 24. Left panel: $[\alpha/M]$ vs. $[M/H]$ contour plots of the thin disk component (75 642 stars, blue), the dissipative collapse component (15 433 stars, red), and the accretion component (1 400 stars, green). Right panel: Galactocentric rotational velocities V_ϕ as a function of $[M/H]$. We only show stars with parallax errors lower than 20%, $S/N > 40$ and "n&o" RAVE classification. We estimated the gradients of V_ϕ vs. $[Fe/H]$ in the thin disk component and in the dissipative collapse component and find good agreement with literature values, despite our different selection criteria (see for example Kordopatis et al. (2011b) and Lee et al. (2011)). We note that the positive gradient of V_ϕ vs. $[Fe/H]$ in the dissipative collapse component results from the superposition of mono- $[\alpha/M]$ sub-populations with negative slopes (Minchev et al. 2019).

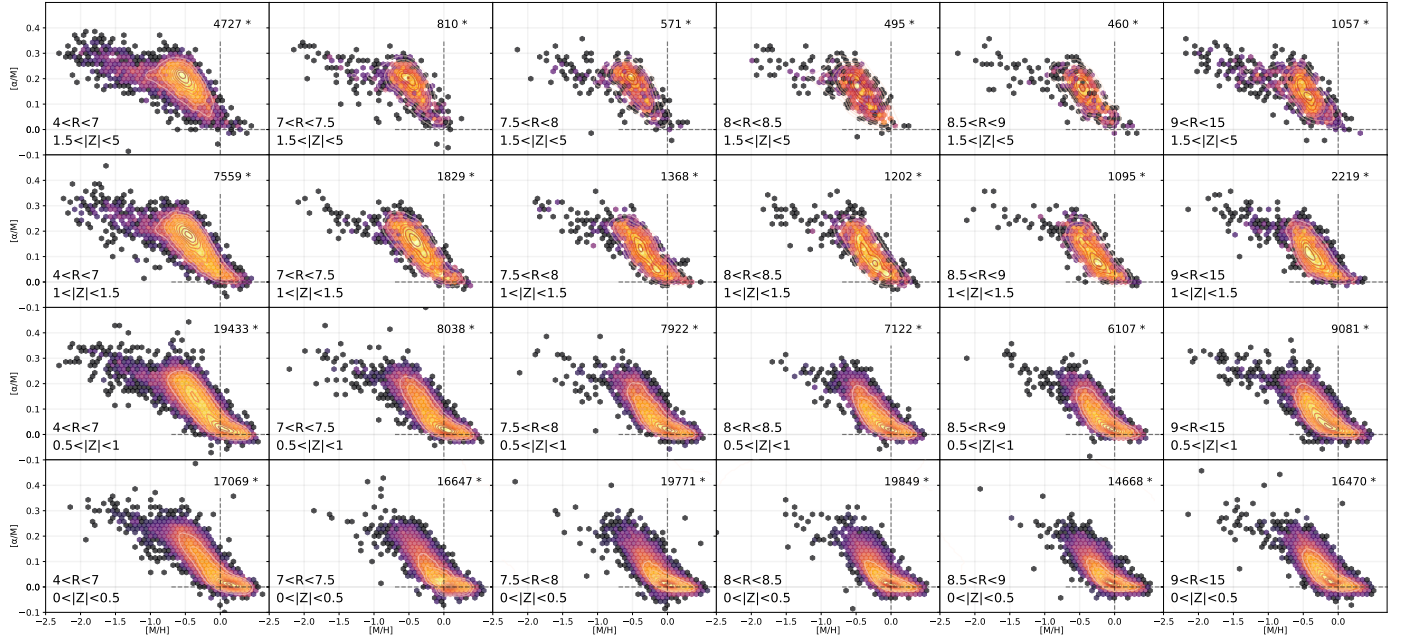


Fig. 25. $[\alpha/M]$ ratio as a function of $[Fe/H]$ for several bins of R and $|Z|$. $[\alpha/M]$ and $[Fe/H]$ were derived through our CNN while the R and $|Z|$ come from the DR6 of RAVE (Steinmetz et al. 2020b). Hexagonal bins and contour plots of the data are presented together. In total, we present trends for 185 569 stars with $S/N > 30$, parallax errors lower than 20%, and RAVE "n&o" classification.

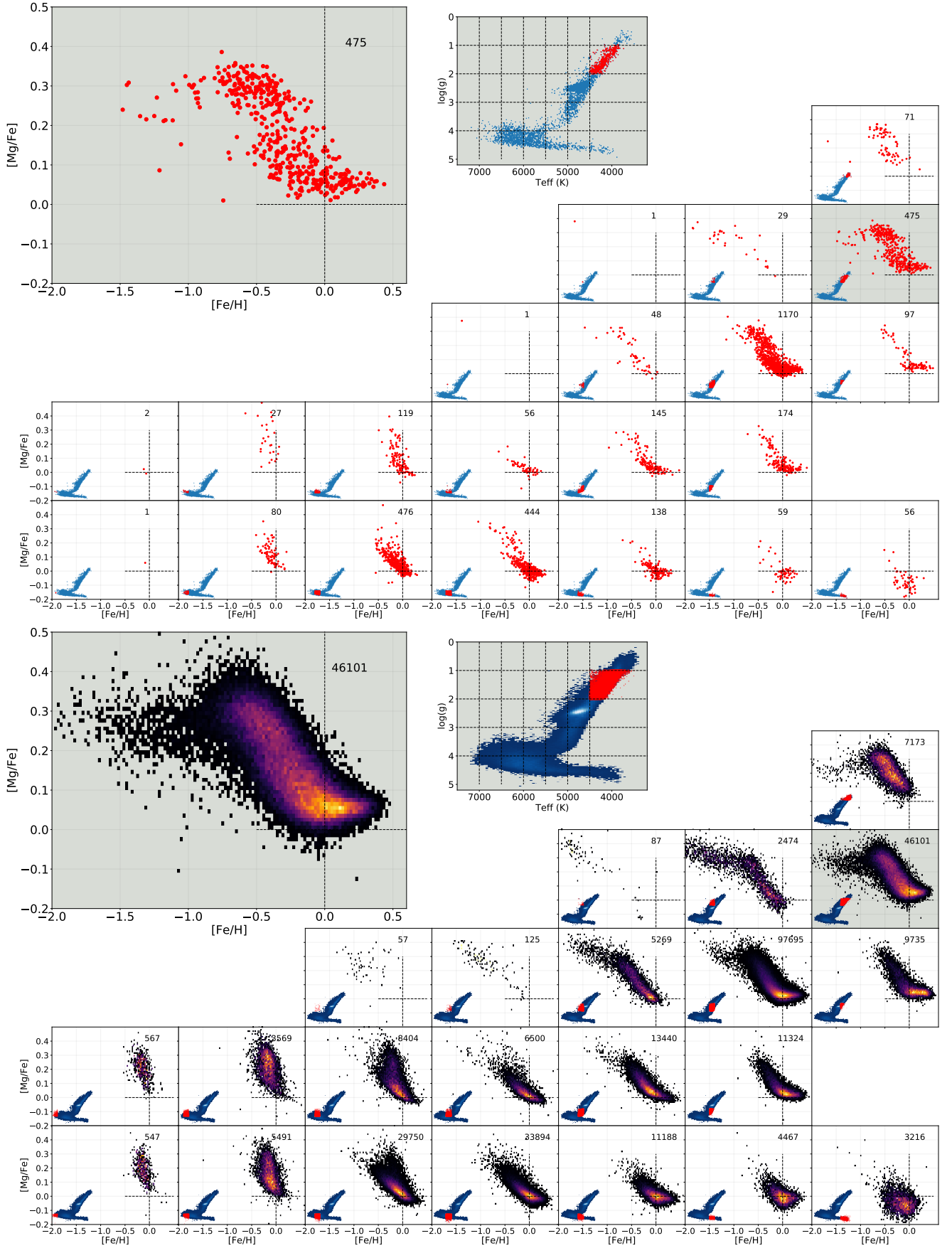


Fig. A.1. Top: $[Mg/Fe]$ vs. $[Fe/H]$ for the training sample. Bottom: $[Mg/Fe]$ vs. $[Fe/H]$ for 301 076 stars of the observed sample with $S/N > 30$, RAVE DR6 "n&o" classification, and parallax errors lower than 20%. For each panel, we overplotted a $T_{\text{eff}} - \log(g)$ diagram with the location of the plotted stars marked in red.

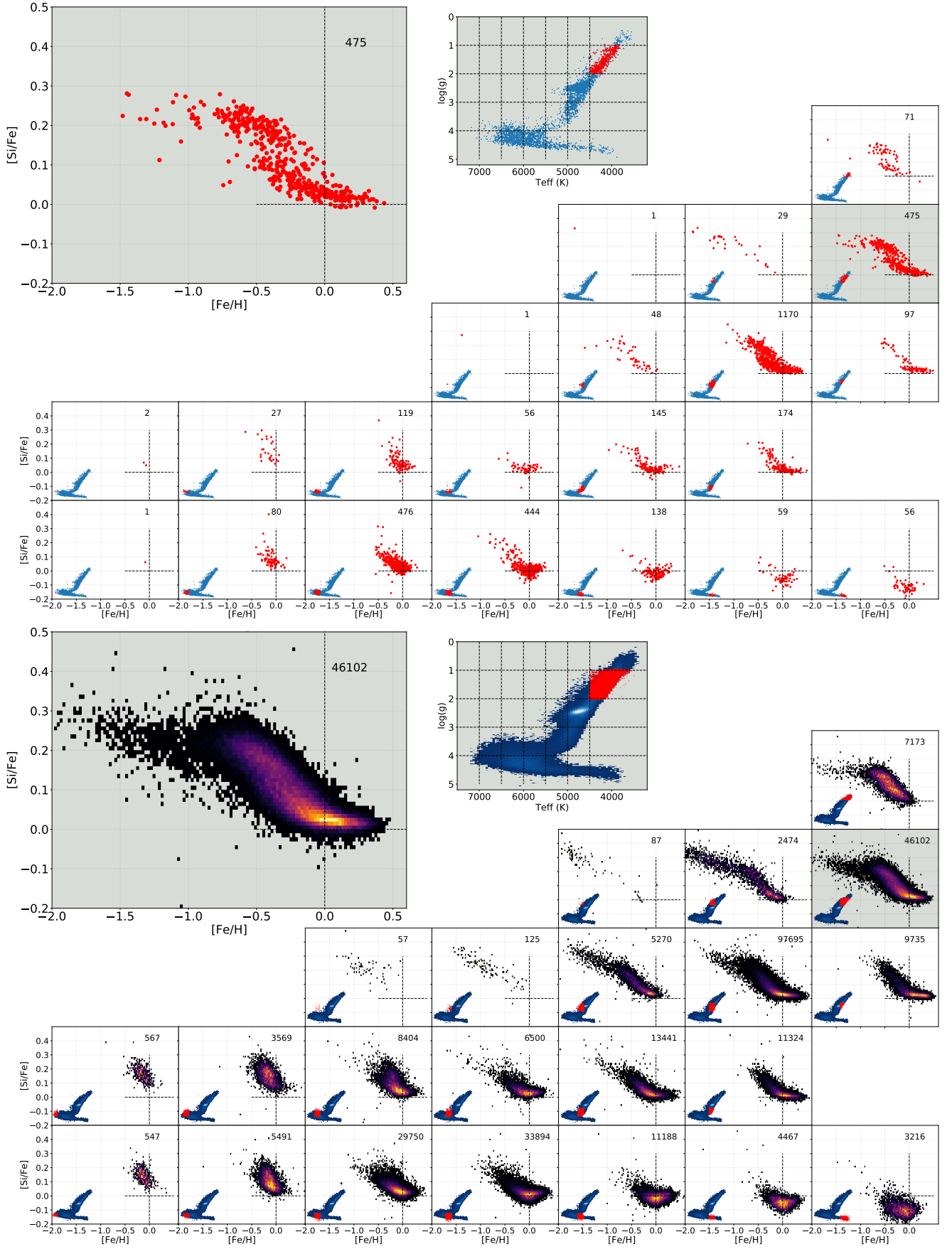


Fig. A.2. Top: $[\text{Si}/\text{Fe}]$ vs. $[\text{Fe}/\text{H}]$ for the training sample. Bottom: $[\text{Si}/\text{Fe}]$ vs. $[\text{Fe}/\text{H}]$ for 301 076 stars of the observed sample with $S/N > 30$, RAVE DR6 "n&o" classification, and parallax errors lower than 20%. For each panel, we overplotted a $T_{\text{eff}} - \log(g)$ diagram with the location of the plotted stars marked in red.

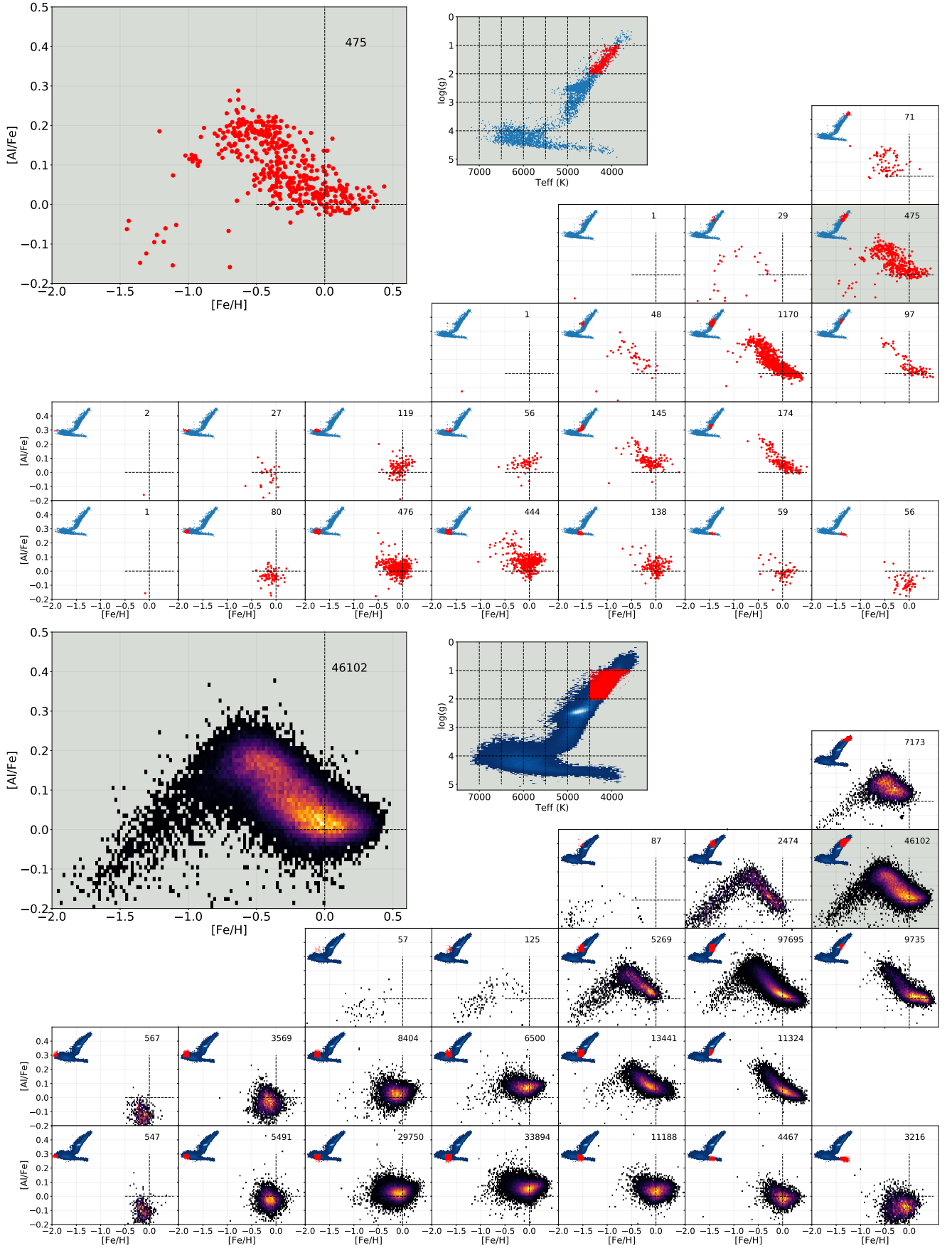


Fig. A.3. Top: $[Al/Fe]$ vs. $[Fe/H]$ for the training sample. Bottom: $[Al/Fe]$ vs. $[Fe/H]$ for 301 076 stars of the observed sample with $S/N > 30$, RAVE DR6 "n&o" classification, and parallax errors lower than 20%. For each panel, we overplotted a $T_{\text{eff}} - \log(g)$ diagram with the location of the plotted stars marked in red.

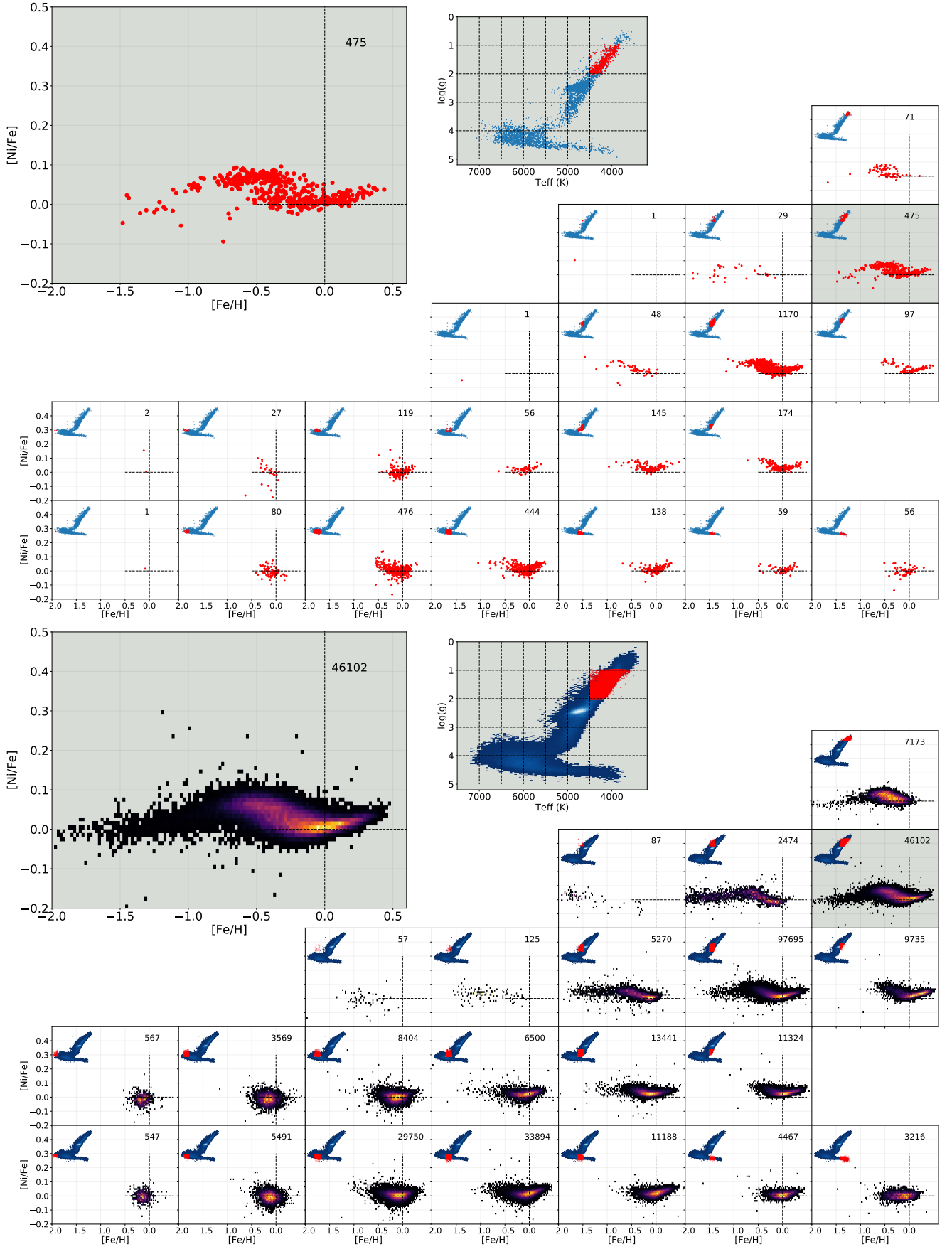


Fig. A.4. Top: $[\text{Ni}/\text{Fe}]$ vs. $[\text{Fe}/\text{H}]$ for the training sample. Bottom: $[\text{Ni}/\text{Fe}]$ vs. $[\text{Fe}/\text{H}]$ for 301 076 stars of the observed sample with $\text{S/N} > 30$, RAVE DR6 "n&o" classification, and parallax errors lower than 20%. For each panel, we overplotted a $T_{\text{eff}} - \log(g)$ diagram with the location of the plotted stars marked in red.